Magma transfer and degassing budget: Application to the 2009–2010 eruptive crisis of Mt Garet (Vanuatu arc)

N. Métrich, A. Bertagnini, E. Garaebiti, S. Vergniolle, Philipson Bani, A. Beaumais, D.R. Neuville

Magma transfer and degassing budget: Application to the 2009–2010 eruptive crisis of Mt Garet (Vanuatu arc)

N. Métrich [a,b,*], A. Bertagnini [b], E. Garaebiti [c], S. Vergniolle [a], P. Bani [d,e], A. Beaumais [f], D.R. Neuville [a]

[a] Institut de Physique du Globe, Sorbonne Paris-Cité, Univ. Paris Diderot, CNRS UMR 7154, F-75005 Paris, France
[b] Istituto Nazionale di Geofisica e Vulcanologia, Sezione di Pisa, Pisa, Italy
[c] Vanuatu Meteorology and Geohazards Department, Port-Vila, Vanuatu
[d] Center for Volcanology and Geological Hazard Mitigation, Bandung, Indonesia
[e] Laboratoire Magmas et Volcans, Univ. Blaise Pascal, CNRS, IRD, OPGC, 63000 Clermont-Ferrand, France
[f] Centre de Recherches Pétrographiques et Géochimiques, 54501 Vandœuvre lès Nancy, France

Mt Garet, on Gaua Island, is one of the active volcanoes of the Vanuatu arc. We report here a new dataset on lapilli and lava erupted during Mt Garet unrest in 2009–2010 and on products of the older activity of Gaua composite volcano. The present-day magma of Mt Garet is a trachy-andesite (52 wt.% SiO_2) with relatively high Rb/Th (14.6) and Ba/La (41) ratios compared to the Gaua pre- and syn-caldera series, but typical of the central part of Vanuatu arc. Its mineral assemblage is mainly composed of plagioclase ($An_{86–56}$) and clinopyroxene ($Fs_{5–16}$) which display significant chemical variations, patchy zones, surface dissolution, and oscillatory zoning that imply episodes of high undercooling and growth rates. The paragenesis is complemented by Fe–Ti oxides and scarce olivine ($Fo_{72–73}$). The melt inclusions are ubiquitous and their compositions cover a chemical spectrum from basalt to trachy-andesite. Volatile-rich basaltic inclusions (H_2O: 2.7 wt.%, S: 0.15 wt.%, and Cl: 0.22 wt.%) are preserved in Mg-rich clinopyroxene whereas the majority of the melt inclusions is volatile poorer with, ≤1.0 wt.% of H_2O, ≤0.05 wt.% of S, and 0.25–0.27 wt.% of Cl. At 1100 °C the measured viscosity of anhydrous magma of Mt Garet is $10^{3.5}$ Pa s. Adding 0.8 to 2.5 wt.% of H_2O decreases the melt viscosity by 0.5 to two orders of magnitude. Com-bining data on bulk rocks, minerals, and their melt inclusions together with the very first published gas fluxes ac-quired during the same period of activity, we propose that the high sulfur outgassing in 2009–2010 was produced by the degassing of a basaltic magma batch (~0.027 km^3) emplaced in a shallow reservoir. This scenario would require temperature and H_2O-loss driven resorption/crystallization, magma mixing, and exsolution of an early gas phase rich in H_2O, and S.
We suggest here the 2009–2010 activity to be sustained by the existence of thermal convection driven at the bot-tom of the magma reservoir by cooling, and in which the bubbles are small enough to be stagnant. The most en-ergetic phases are better explained by an additional gas volume, associated to the crystallization of titanomagnetite microcrysts which significantly enhance bubble nucleation. The ultimate step of crystal growth prior to eruption suggests magma ascent within few hours.

1. Introduction

The Vanuatu island arc, in the Southwest Pacific, is known for its very active and large volcanoes as those on Ambrym Island (Németh and Cronin, 2008) and for the permanent strombolian/vulcanian activity of Yasur (Tanna island) which was first reported by Captain Cook in 1774 (e.g., Aubert de la Rüe, 1960). Recent airborne measurements of SO_2 emission rates, between 2009 and 2012, indicated that the Vanuatu arc is one of the prominent sources of volcanic degassing on Earth (Bani et al., 2012). The very first and only data set presently available for Mt Garet, the active cone of Gaua Island in the central segment of Vanuatu arc, revealed a high SO_2 flux of, on average, 2959 t per day in October–December 2009 period of activity (Bani et al., 2012).

Mt Garet is a 460 m high cone that is built up within the summit caldera of a large composite volcano. It was covered by a forest until 1962 when a long period of rest, dated back at least to 1868, ended (Mallick and Ash, 1975). Since 1962, Mt Garet has recurrently produced ash, white steams and gas plumes, and the water of Lake Letas has been periodically discolored (e.g., Mallick and Ash, 1975; Bani et al., in this volume). The last intense explosive activity was documented in 2009–2010, with repeated emissions of several km-high ash-laden plumes, which forced the evacuation of villages located downwind to the trade winds. Since Mallick and Ash (1975), very few data have been published on Gaua volcanic products (e.g., Robin et al., 1995; Peate et al., 1997;

* Corresponding author at: Institut de Physique du Globe de Paris, Bureau 438, 1, rue Jussieu, 75238 Paris, Cedex 05, France.
E-mail address: metrich@ipgp.fr (N. Métrich).

Beaumais et al. in this volume), and nothing was known about the present-day magmas of Mt Garet.

The present work provides a comprehensive dataset on the geochemistry and mineralogy of the Mt Garet magma, which erupted explosively in 2009–2010, and aims at deciphering the degassing processes that led to high SO_2 emissions and ash clouds. We report here also a new sampling of the pre- and syn-caldera activities of Gaua stratovolcano. Our sample set has provided the opportunity to build up a coherent database on geochemistry and mineralogy of the 2009–2010 products, and, for the first time, has shed light on the present-day volcanic activity of Mt Garet in the framework of Gaua volcano.

2. Geological background and sampling

Gaua Island, originally called Santa Maria (Mallick and Ash, 1975), is located in the central segment of the Vanuatu arc (Fig. 1), where the D'Entrecasteaux ridge — a 100 km wide Eocene–Oligocene island arc complex on the Australian subducting plate collides with the fore-arc (e.g., Collot et al., 1985) and the sub-marine West Torres Plateau is subducted (Meffre and Crawford, 2001). Arc-ridge collision, facing deep back-arc basins, is thought to be responsible of crustal shortening (Pelletier et al., 1998) and slow down of the convergence rate at the plate boundary (e.g., Baillard et al., 2013). Gaua lies on the northern edge of Aoba back-arc basin, ca. 200 km above the surface of the slab which dips at ca.70° (e.g., Syracuse and Abers, 2006). The island is formed by a large Pleistocene–Holocene composite volcano, of approximately 2400 m in height, with a summit caldera (6×9 km; Mallick and Ash, 1975). The pre-caldera activity of Gaua volcano mainly produced basalts and andesites (Mallick and Ash, 1975). The caldera formation has been related to a phreatomagmatic eruption and massive discharge of a chemically layered magma chamber (Robin et al., 1995) or a process of slow, non-explosive subsidence (Mallick and Ash, 1975) as also discussed in the case of Ambrym volcanoes (Németh and Cronin, 2008). Mt Garet emerges from the Lake Letas that fills the volcano summit caldera (Fig. 1).

Lava and pyroclastic rocks representing different periods of activity of Gaua volcano were collected during a field mission in September 2010 (Fig. 1). Following Mallick and Ash (1975), the pre-caldera stage samples were collected from (i) the strombolian scoria fall deposits of Burilan and Devil Rock littoral cones (Gaua 9b, 11, 12a), and (ii) a pyroclastic flow deposit of white pumice (Gaua 14), which was observed for the first time in a ca. 10-m thick succession of ash and scoria layers, cropping out along the sea near Bushman bay, on the west coast. We also sampled blocks of obsidian (Gaua 21) and banded pumice (Gaua 22) at the river mouth at Losolava village, along the northeast coast. Obsidian blocks were first attributed to the syn-caldera plinian phase by Robin et al. (1995). Although the stratigraphic position of these samples is unknown, they come most likely from a fallout deposit in the caldera wall. They differ in texture and composition (as detailed hereafter) from the juvenile fraction of the syn-caldera pyroclastic flow deposits and could instead belong to the pre-caldera stage.

The juvenile components, as well preserved scoriae and bread-crust bombs, of recent pyroclastic flow deposits were sampled (Gaua 17, 24, 25b) along the northern coast at Bushman Bay, where they are well exposed. These deposits were ascribed to the large caldera-forming eruption by Robin et al. (1995).

Ankaramites (Gaua 4), recognized for long time on Gaua (Mallick and Ash, 1975), are emplaced as lava flows on the SW coast. They were not attributed to a precise period of the stratovolcano activity because of the absence of unequivocal stratigraphic relationships between the deposits. Other samples of lava flow (Gaua 2) and associated cone (Gaua 3) near Ontar village on the SW coast, which were previously described as ankaramites, are basaltic trachy-andesites as proved by chemical analyses (Table 1).

The lapilli and lava blocks of 2009–2010 explosive activity of Mt Garet were collected during the eruptive crisis which was preceded by strong gas release that caused the complete burning of vegetation on the NW sector of the cone. The first eye-witness accounts, on 29 September 2009, reported strong explosions propelling an ash laden, umbrella-shape plume, which could have reached 3 km in height. In the following two months many explosions associated with ash emissions were recorded by a seismic station installed on the island and observed by the inhabitants (Bulletin of the Global Volcanism Network, 2009). Since mid-December the ash emissions were continuous and ash fallouts significant. In January–February the explosive activity increased culminating in stronger explosions on 27th and 29th of January and 4th of February (Bulletin of the Global Volcanism Network, 2009). Emission of ash plumes is reported until June 2010 (Bulletin of the Global Volcanism Network, 2010). Scoria lapilli emitted early 2010, which were accumulating along shores of Lake Letas (Gaua 27A) and floating on the lake surface (Gaua 27B), were sampled on 4th of

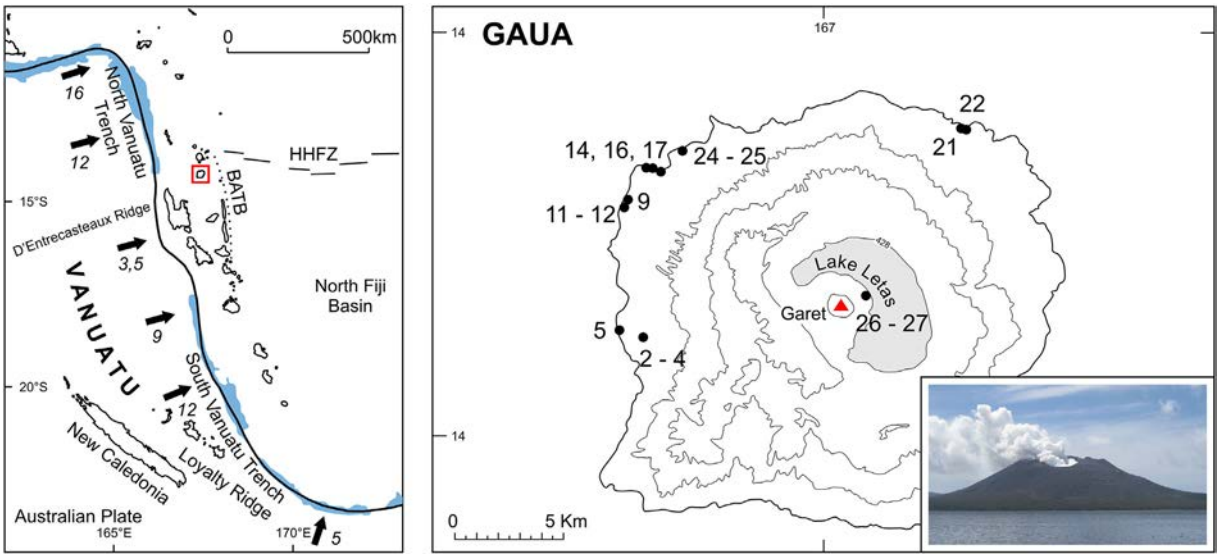

Fig. 1. Map showing Vanuatu (previous New Hebrides) arc in southwest Pacific, the convergence rates (indicated by arrows in cm year^{-1}), and the location of Gaua volcanic island redrawn from Pelletier et al. (1998), and Calmant et al. (2003), on the left. Schematic map of Gaua Island redrawn from Beaumais et al. (in this volume) with the 2010 sampling sites on the right. The photograph by E. Garaebiti shows Mt Garet and Lake Letas on 30 September 2010.

Table 1
Chemical compositions of Gaua bulk rocks.

Locality coordinates	Present-day activity		Pyroclastic series			Pre-caldera activity										
	Mt Garet		Bushman Bay			Devil rocks	Burilan		Aro	Bush. Bay	Losolava		Ontar area			
			S14°13′35.4″	S14°13′21.4″		S14°14′59.9″	S14°24′39.3″		S14°13′33.7″	S14°13′29.8″	S14°12′63.0″		S14°17′27.2″			S14°17′58.1″
			E167°26′29.7″	E167°27′05.4″		E167°25′28.7″	E167°30′48.1″		E167°26′07.0″	E167°26′14.1″	E167°33′99.2″		E167°26′14.1″			E167°25′41.7″
Sample	Gaua 26	Gaua 27B	Gaua 17	Gaua 24	Gaua 25b	Gaua 12a	Gaua 9b	Gaua 11	Gaua 14	Gaua 16	Gaua 22	Gaua 21	Gaua 2	Gaua 3	Gaua 4	Gaua 5
Type	Lava	Lapilli	Scoriae	Scoriae	Scoria [1]	Lava block	Scoriae	Scoriae	Pumice	Lava	Pumice	Obsidian	Scoria	Lava	Lava	Lava
SiO_2 (wt.%)	52.12	52.25	50.41	51.16	51.01	48.79	50.78	52.02	57.16	52.29	60.22	63.67	52.11	51.81	46.43	46.68
Al_2O_3	16.45	16.55	16.59	16.68	16.61	12.81	16.74	17.09	17.11	18.35	16.98	16.63	16.51	16.77	11.18	12.49
Fe_2O_3	10.36	10.19	10.89	10.93	10.93	11.14	10.56	9.39	6.22	9.40	4.35	4.09	10.18	10.34	11.23	11.96
MnO	0.19	0.19	0.23	0.22	0.23	0.19	0.22	0.22	0.20	0.20	0.14	0.14	0.22	0.23	0.19	0.19
MgO	4.69	4.57	3.96	3.95	4.21	8.27	4.05	3.49	1.68	3.11	0.75	0.67	4.06	3.41	15.76	12.46
CaO	9.76	9.70	8.60	8.27	8.56	12.63	8.64	7.17	3.98	8.50	1.62	1.67	8.25	7.35	10.82	12.39
Na_2O	3.14	3.14	3.62	3.45	3.83	2.56	3.65	3.82	5.11	3.95	5.56	5.62	3.73	3.70	1.77	1.84
K_2O	1.70	1.73	2.09	1.91	2.15	1.66	2.05	2.61	3.99	2.42	5.20	5.62	2.54	2.68	0.81	0.65
TiO2	0.72	0.72	0.85	0.85	0.85	0.76	0.82	0.76	0.58	0.77	0.50	0.49	0.80	0.82	0.67	0.77
P_2O_5	0.21	0.20	0.40	0.37	0.41	0.27	0.32	0.35	0.29	0.43	0.16	0.16	0.38	0.38	0.15	0.15
L.O.I.[2]	−0.24	−0.03	1.60	2.22	0.73	0.76	1.23	2.15	3.34	0.00	4.10	0.64	0.08	1.05	0.23	−0.04
Total	99.09	99.20	99.24	100.00	99.50	99.85	99.07	99.07	99.66	99.43	99.56	99.39	98.85	98.53	99.23	99.55
Sc (ppm)	26.4	20.3	20.1	19.8	19.6	36.8	19.6	15.5	7.6	15.6	5.9	5.3	21.2	21	35.9	39.9
Cr	20	18	4	4	5	290	5	5	4	5	3	5	8	4	915	641
Co	34.3	31	34.7	34	34.2	44.6	33.9	28.7	12.4	27.2	6	4.4	32	31.9	66.5	59.6
Ni	25	23	12	11.6	12.9	57	12.4	13	2.1	14	5	3.1	18	16	377	228
Rb	30.1	32.4	37.2	33.8	36.8	22.7	36.8	46.3	74.6	37.4	100.4	105	35.3	42	10.5	9.9
Sr	576	603	879	844	841	729	903	918	658	1024	224	219	846	780	527	543
Zr	86	78	94	97	96	69	81	107	164	106	240	223	103	113	46	40
Sb	0.1	0.12	0.15	0.12	0.11	0.058	0.12	0.15	0.21	0.098	0.34	0.33	0.091	0.09	0.039	0.027
Cs	0.56	0.63	0.52	0.49	0.5	0.216	0.47	0.6	1.03	0.18	1.49	1.55	0.32	0.22	0.034	0.022
Ba	430	462	544	519	539	428	513	636	941	598	1006	1070	688	713	256	172
La	10.52	11.25	19.08	18.16	19.44	13.85	17.77	21.45	27.21	20.53	28.99	28.52	21.19	29.56	7.66	7.01
Ce	24.3	25.3	43.7	41.1	41.2	29.9	39.5	50.1	60.1	45.4	63.6	62.4	46.2	54.5	17.7	16.6
Nd	14.1	14.3	24.3	27.1	26.9	15.2	23.1	26.5	31.4	29.2	35.3	31.5	25	32.5	13.5	11.1
Sm	3.75	3.77	5.72	5.46	5.59	4.15	5.3	5.64	6.43	5.81	5.87	5.75	5.96	7.2	2.92	3.01
Eu	1.11	1.07	1.73	1.65	1.69	1.25	1.63	1.63	1.73	1.78	1.3	1.38	1.7	1.99	0.96	0.98
Tb	0.530	0.524	0.698	0.660	0.677	0.487	0.630	0.636	0.752	0.673	0.722	0.703	0.709	0.851	0.379	0.404
Yb	2.22	2.2	2.65	2.49	2.56	1.57	2.33	2.39	3.24	2.5	3.78	3.54	2.69	2.39	1.34	1.43
Hf	2.52	2.54	2.85	2.86	2.78	1.9	2.7	3.32	4.78	2.93	6.7	6.28	3.28	3.37	1.36	1.28
Ta	0.106	0.115	0.136	0.135	0.13	0.0836	0.127	0.171	0.255	0.143	0.329	0.306	0.16	0.163	0.0655	0.073
Th	2.08	2.20	2.97	2.92	2.85	2.10	2.65	4.07	5.36	3.13	8.10	7.60	3.68	3.77	0.98	0.74
U	0.91	0.94	1.27	1.04	1.1	0.74	1.06	1.39	2.07	1.14	3.28	2.99	1.03	1.31	0.41	0.28

[1] Single scoria.
[2] Loss of ignition.

February 2010 by Gill Jolly (GNS Science, Wairakei Research Centre, New Zealand). In complement we sampled very fresh lava blocks (Gaua 26), in the lower part of the talweg cutting the cone. Soon after the eruption, the lapilli were rapidly flushed in the river connected to Lake Letas and transported in the sea.

3. Analytical and experimental procedures

3.1. Chemical analysis of bulk rocks

A total of 16 samples (lavas, scoriae and pumices) of the Gaua volcano pre- and syn-caldera activity, in complement to the dataset reported in Beaumais et al. (in this volume), and of the 2009–2010 activity of Mt Garet were analyzed for major and trace elements. Bulk rock powders were analyzed for trace elements using instrumental neutron activation (CE-Saclay Osiris reactor, France) and γ-spectrometry. The relative standard deviation (RSD%), calculated over 14 years for the basaltic standard BE-N (300 analyses), is <3% for most elements (except for Eu: 5%, and for Rb and Zr: 6%) (Joron et al., 1997). Major element concentrations were measured at the Service d'Analyse des Roches et Minéraux (CRPG-CNRS, Nancy, France), by using Inductively Coupled Plasma Optical Emission Spectroscopy (Thermo Fisher ICap 6500), and trace element concentrations in a sub-set of the samples using Inductively Coupled Plasma Mass Spectrometry (Agilent 7700X). The RSD values for trace elements vary from <15% (Ta, U) and <10% (Th, Nb, Hf, Zr) to <5% (Ba, Sr, Rb, REE). They are <2% for K, Na, Mg, Ca, and Ti and <1% for Si, Al, and Fe. The trace analyses have been cross-checked and the whole data set is consistent, as shown further.

3.2. Minerals, melt inclusions, and matrix glasses

In Gaua 27A, minerals were handpicked in the grain size fractions 1–2 mm and 0.5–1 mm, after lapilli gentle grinding. In Gaua 26, mineral study was carried out on thin section. Crystals were mapped and their zoning patterns characterized using a scanning electron microscope Zeiss EVO MA 10 (INGV, Pisa, Italy). They were analyzed using a SXFive CAMECA electron probe (Camparis, Paris, France), with a beam current of 10 to 20 nA and counting time from 10 to 25 s. Chemical profiles were obtained with steps of 20 μm and of 5–6 μm in the zones of specific interest. Some Fe–Ti oxides were analyzed with electron microscope Zeiss EVO MA 10. We checked that SEM and EMP analyses were comparable (see Section 4.2).

Glass and melt inclusion compositions were determined using a 10 nA defocused beam and a counting time on peak varying from 10 to 25 s for major elements, and of 200 s for minor elements (S, Cl, P). Sodium was counted first to avoid any damage along the analysis. Accuracy and reproducibility of major element analyses were checked on reference glasses (Supplementary material Table S2), as did S and Cl measurements [VG2 basaltic glass for Cl: 310 ppm and S: 1458 ppm (Jenner and O'Neill, 2012) and KE12 pantellerite for Cl: 3340 ± 60 ppm (Métrich and Deloule, 2014)]. We measured 288 ± 17 ppm of Cl, and 1430 ± 17 ppm of S for basaltic glass VG2 and 3373 ± 31 ppm of Cl for pantellerite glass KE12. The relative errors are ≤7% for S and Cl and their detection limits are 40 and 45 ppm, respectively.

The dissolved H_2O contents were measured with micro-Raman spectroscopy, using a T64000 Jobin-Yvon triple grating Raman spectrometer (IPG-Paris, France) equipped with a confocal system, a 1024 CCD detector cooled by liquid nitrogen and an Olympus microscope. The optimal spatial resolution allowed by the confocal system is 1–2 μm^2 with a 100× Olympus objective. The spectral resolution of the spectrometer is 0.7 cm^{-1}. Samples were excited with a Coherent laser 70-C5 Ar+, having a wavelength of 514.532 nm. The LASER power delivered to the sample varied from 100 to 250 mW. The data and spectra are treated following Le Losq et al. (2012). Calibration was made on glass standards, previously developed for Raman, which cover a very large range of chemical composition from basalts to dacites and alkali-rich synthetic glasses and H_2O concentrations from 0.4 to 4 wt.% (Mercier et al., 2009; Le Losq et al., 2012). This method is thought to be independent on the sample chemical composition and on the acquisition conditions, and allows a good reproducibility (0.2 wt.%; Le Losq et al., 2012).

3.3. Optical thermometry

The temperatures of melt entrapment were determined from optical thermometry measurements on fully enclosed, bubble-free melt inclusions hosted in plagioclase of the 2010 scoriae. Experiments were carried out under the Linkam TS1500 heating stage (IPG-Paris, France). Temperatures were measured with a Pt-$Pt_{90}Rh_{10}$ thermocouple (±10 °C), and calibrated against the melting points of Ag (961.8 °C) and Au (1063.8 °C). The rates of temperature increase were 25 °C per minute until 920–940 °C and then 1 °C per minute until homogenization. As a whole a total of 5 heating experiments were conducted on double-faced polished crystals whose inclusions were preserved enclosed. The homogenization temperatures (T_{hom}), when the contraction bubble disappears, vary from 1087 to 1131 °C and average at 1108 ± 10 °C.

3.4. Viscosity measurements

Viscosity measurements were carried out on the Gaua 26 lava sample. About 10 g of natural sample were cleaned, crushed in an agate mortar, melted in a Pt crucible at 1650 °C and quenched in water. The Gaua 26 glass was annealed 2 days at 400 °C and finally drill to prepare 5 mm diameter sample for viscosity measurements which were carried out in air, with the creep apparatus described by Neuville (2006). Measurements were repeated between 20 and 40 times at each temperature. Uncertainty and the reproducibility were given by Neuville (2006) by using NBS710 glass sample and are better than 0.03 log units. Within the range of stress applied in the creep experiment (6.6 to 8.9 log Nm^{-2}), the viscosity of the samples is always Newtonian.

4. Results

4.1. Bulk rocks

Major and trace element analyses of bulk rocks are reported in Table 1 and as Supplementary material Table S1.

Ankaramites, and specifically the sample Gaua 4, have been proved, on the basis of melt inclusion data hosted in olivine Fo_{90-92}, to be representative of true ankaramitic melts involving clinopyroxenite (± amphibole) lithology in the magma source (Sorbadere et al., 2013a). Leaving apart ankaramites, Gaua pre- and syn-caldera bulk rocks belong to potassic calk-alkaline series and covered a wide range of chemical compositions from basalts to trachy-dacites. Their content in SiO_2 varies from 48.8 to 63.7 wt.% and MgO from 8.3 to <1 wt.% and they define an almost continuous trend (Fig. 2) in agreement with Beaumais et al. (in this volume). The Si-rich end-member of Gaua series is represented by trachy-dacitic obsidian blocks (Gaua 21). The new samples collected from the last syn-caldera pyroclastic flows plot along the general trend. We underline that ICP-MS and INAA results for trace elements are fully comparable (Fig. 2; Supplementary material Table S1).

The 2009–2010 basaltic andesites of Mt Garet depart from this general trend in having relatively lower Th concentrations and significantly higher Rb/Th (14.6), and Ba/La (41) ratios and a higher Ba content (Fig. 2a–c). The two present-day samples of Mt Garet have exactly the same composition in major and trace elements (except Pb) despite their textural difference. They share comparable concentrations in MgO (4.6 wt.%) and CaO/Al_2O_3 ratio (0.59) with the Mt Garet pre-1962 basalts but they are relatively and significantly enriched in incompatible elements. In fact they plot between the pre-1962 products and the syn-

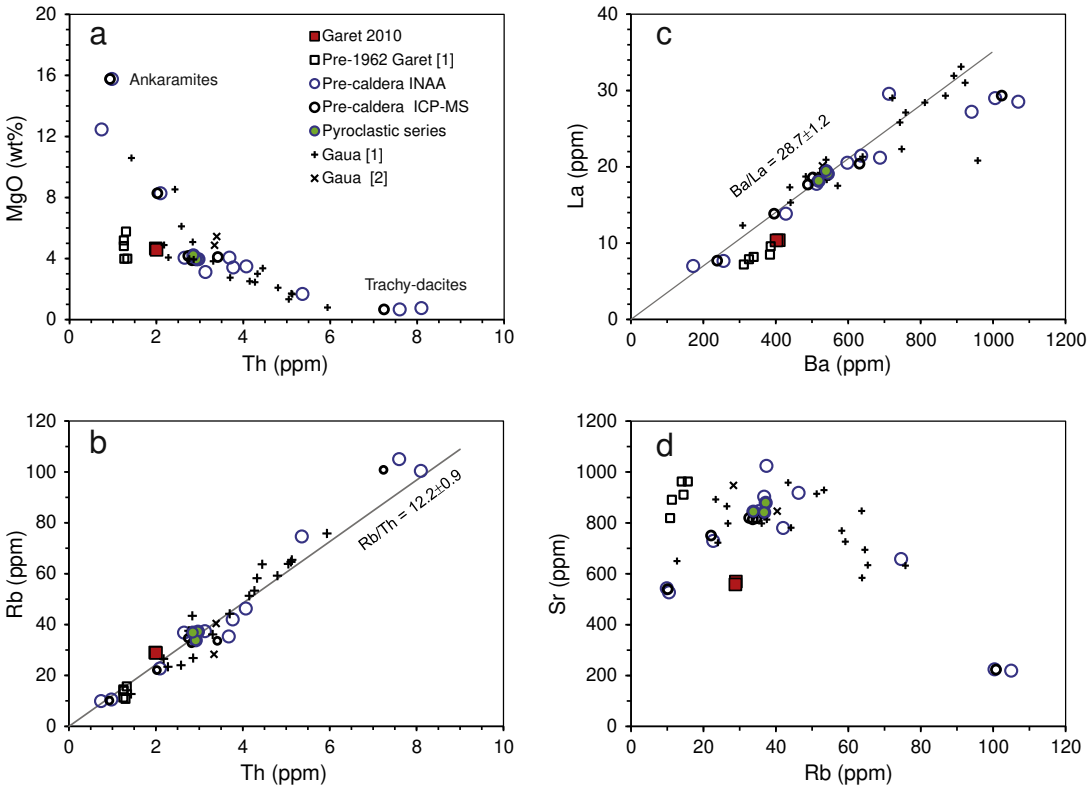

Fig. 2. Evolution of MgO and trace elements in bulk lavas and pyroclastites of the 2009–2010 explosive eruption at Mt Garet and of the pre- and syn-caldera stages of Gaua stratovolcano. Data of both instrumental neutron activation (Table 1) and Inductively Coupled Plasma Mass Spectrometry (Supplementary material Table S1) are plotted. The errors bars are within the symbols. The so-called pre-1962 Garet samples are undated but they preceded the volcano unrest initiated in 1962. The pyroclastic series are ascribed to the large caldera-forming eruption (Robin et al., 1995), caldera in which the Mt Garet has been built. [1] refers to the Gaua pre- and post-caldera samples from Beaumais et al. (in this volume), and [2] to the Gaua stratovolcano early activity dated at 1.7 Ma from Peate et al. (1997).

caldera pyroclastic samples. They also differ by their relatively lower Sr concentration, Sr/Rb ratio and Sr isotope composition (^{87}Sr / ^{86}Sr = 0.704027 ± 6 × 10^{-6} for Gaua 26) from pre-1962 basalts which are, in contrast, abnormally enriched in Sr (Fig. 2d), and radiogenic ^{87}Sr (^{87}Sr / ^{86}Sr mean = 0.704165 ± 3 × 10^{-6}; A. Beaumais, unpub. data). These latter basalts display high Al_2O_3 concentration which achieves 18.4 wt.%. Their concentrations in Sr and Al_2O_3 are positively correlated that could indicate the possible influence of plagioclase.

4.2. Rock textures and their minerals

The lapilli and lava blocks of the present-day activity of Garet cone are characterized by phenocrysts and microphenocrysts of plagioclase, clinopyroxene, and subordinate olivine. Fe–Ti oxides are present as microphenocrysts and solid inclusions in the other phases. The lapilli samples have a vesicular, glassy matrix with no or only rare quenched microlites, and the lava samples display a crystallized and oxidized matrix with millimeter-sized, coalesced bubbles.

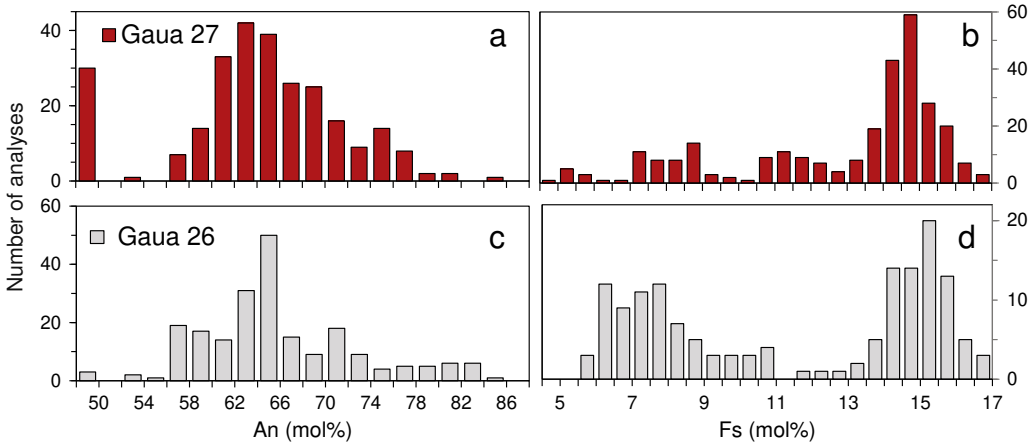

Fig. 3. Distribution of the compositions of plagioclase (a, c) and clinopyroxene (b, d) in the lapilli (Gaua 27) and lava block (Gaua 26) of the 2009–2010 activity of Mt Garet. In the plot 3a, it must be noted that, in Gaua 27 lapilli, the sodic compositions (An < 50) correspond to plagioclase xenocrysts.

The entire dataset for mineral compositions is provided as Supplementary materials (Tables S3, S4, and S5). For each crystal the chemical variation is expressed in mol% of anorthite [100 × Ca / (Ca + Na + K)] for plagioclase, ferrosilite [100 × Fe / (Ca + Mg + Fe)] for clinopyroxene, and forsterite [100 × Mg / (Mg + Fe)] for olivine. In the lapilli (Gaua 27A) both the plagioclase ($An_{85.9–56,}$ with a mode at $An_{62–74}$; Fig. 3a), and the clinopyroxene ($Fs_{5– < 17}$, with a mode at $Fs_{14–16}$; Fig. 3b) are widely zoned. The paragenesis is completed by Fe–Ti oxides ([Fe^{2+} / Fe^{3+}] ratio from 0.63 to 0.59), and olivine ($Fo_{72.3–73.3}$; on average 72.7 ± 0.3). Phenocrysts An ≤ 50 contain decrepitated melt inclusions and display resorption features that prove their mechanically entrainment from the surroundings during the 2010 explosive event. Patchy zoned diopsidic clinopyroxene ($Fs_{4.9–5.2}$; Mg# [Mg / (Mg + Fe)] 0.907–0.902), with Cr_2O_3 content up to 0.8 wt.%, is regarded as antecryst, which did not crystallize in the carrier magma but grew in genetically related parent magma and was further recycled (e.g., Davidson et al., 2007).

Similar features are observed in their equivalent denser lava block Gaua 26. Plagioclase ($An_{84.2–53.0,}$ with a mode at $An_{62–74}$; Fig. 3c) shows systematic concentric zoning, sieve textured and patchy zoned bands and cores. Microlites have a restricted chemical range ($An_{55.7–59.7}$). Clinopyroxene covers the chemical spectrum (Mg# 0.893–0.715; $Fs_{5.6–16.7}$) with two modes (Fig. 3d) and displays the zoning pattern described in the lapilli Gaua 27A. Fe–Ti oxides registered significant variations in their [Fe^{2+} / Fe^{3+}] ratios from 0.64 to 0.57. SEM and EMP analyses of Fe–Ti oxides are similar (Supplementary material, Table S5 and companion figures). Olivine composition is homogeneous ($Fo_{72.6–73.5}$; on average 73.1 ± 0.2).

Plagioclase, in samples Gaua 27 and 26, shows An-rich patchy zoned cores embedding large glass inclusions, and systematic oscillatory

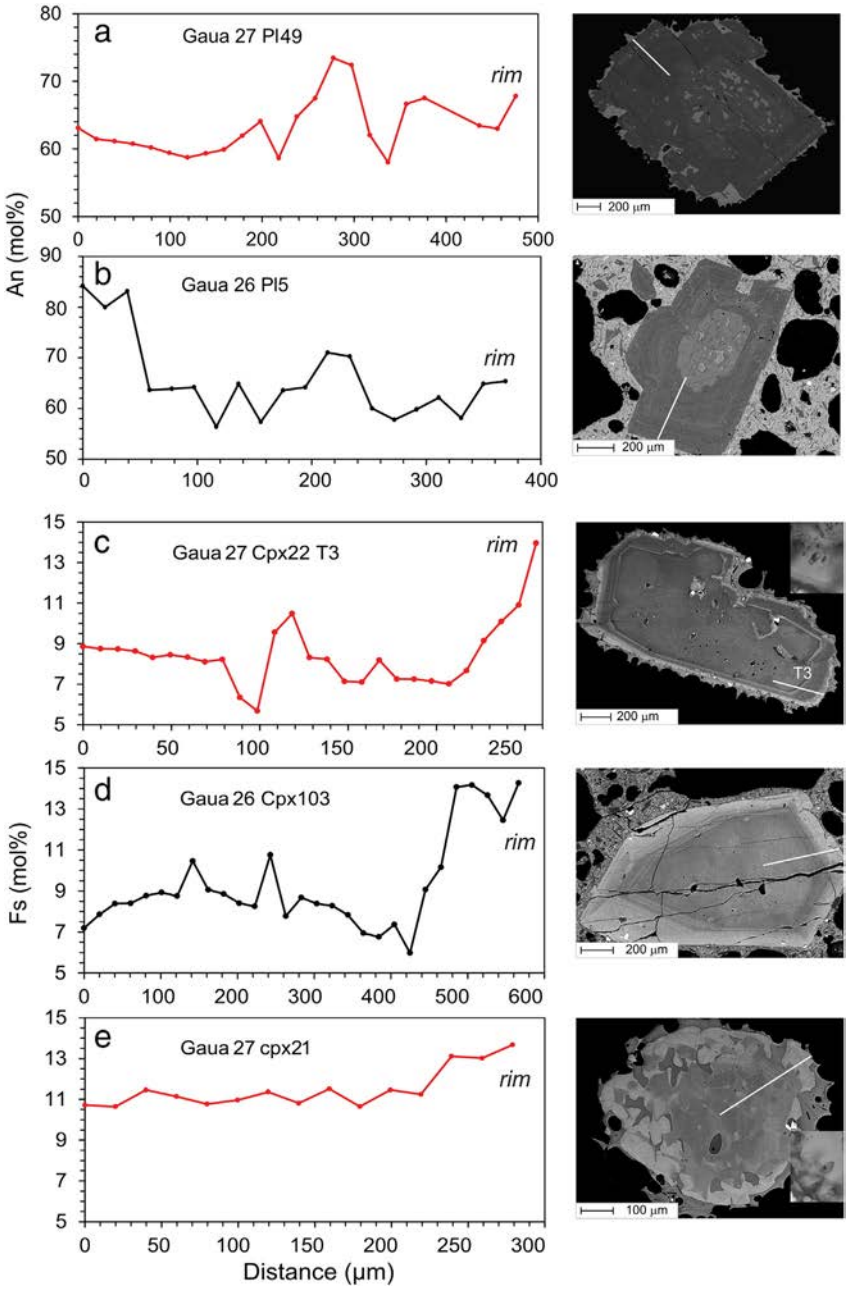

Fig. 4. Electron microprobe chemical profiles in selected plagioclase and clinopyroxene phenocrysts of lapilli Gaua 27 and lava block Gaua 26 with the associated BSE images of the crystals. In each image, the white line symbolizes the profile along which the EMP analyses have been done. Note the sector zoning on pyroxene rims in c and d. The inset in c (upper-right corner) and e (lower-right corner) shows typical melt inclusions.

zoning (Fig. 4a, b). Plagioclase textures testify to an early stage of crystallization as well illustrated in Fig. 4b showing that the An-rich core originated from synneusis and growth of several nuclei. In addition, the composition of the darker patches (An_{75}) in the core and more importantly the sharp interface and abrupt chemical jump from An_{84} to An_{64} bands are consistent with a process of crystallization into open spaces of skeletal crystals rather than resorption or diffusional re-equilibration of inherited xenocrysts (Humphreys et al., 2006; Streck, 2008 and references therein). The plagioclase cores are surrounded by oscillatory zoning layers with a thickness from a few to several tens of μm (Fig. 4a, b), and a narrow compositional range (An_{58-64}, and An_{56-66}; Table S3). Many of the dark gray layers (low An content) are interrupted or undulated revealing minor episodes of resorption before the growth of light gray, An-richer layers that reach composition An > 80. These textural characteristics suggest that the oscillatory zoning are related to minor and repeated fluctuations of P-T conditions and/or magma H_2O content rather than to kinetic effects (Ginibre et al., 2002, 2007; Humphreys et al., 2006). In contrast, the presence of thicker, An-rich layers (up to An_{84-86}) reveals larger amplitude variations of physical and chemical parameters. Some of them show coarse sieve textures embedding glass inclusions and clearly grew after an episode of strong dissolution of a more sodic layer (Fig. 4a). Partial resorption of An-poor plagioclase, due to magma refilling and mixing, and then rapid skeletal growth of An-rich composition during degassing are observed at many volcanoes (e.g., Landi et al., 2004; Shiveluch volcano, Humphreys et al., 2006).

Changes in clinopyroxene composition are associated with patchy zoned cores, small scale oscillatory zoning (width of individual oscillations <20 μm), concentric growth bands of >20 μm thickness, and sector zoned rims. The BSE image and chemical transect in Fig. 4c provide a good summary of the crystal growing steps in illustrating successive features that include (i) a slightly patchy zoned core surrounded by a resorption surface ($Fs_{8.5 \pm 0.3}$; $Cr_2O_3 = 0.19 \pm 0.02$; N = 35), (ii) a growing diopsidic band ($Fs_{5.7}$; $Cr_2O_3 = 0.59 \pm 0.02$), (iii) a thin Fe-rich layer ($Fs_{9.6}$), (iv) an oscillatory zone with composition from $Fs_{7.1}$ to $Fs_{8.2}$, and finally (v) sector zoned rims (up to Fs_{14}). Another 250 μm profile (Transect1; Table S4) provides similar information. These features are inconsistent with a single process of crystal fractionation, but infer changes of magma crystallization conditions. Sharp increase in the FeO content ($Fs_{5.7\ to}\ Fs_{9.6}$), associated with Cr_2O_3 decrease from 0.59 to 0.17 wt.%, could testify very rapid high Mg# clinopyroxene crystallization from a more primitive volatile-rich magma batch, and no time for Fe–Mg diffusion. It is interpreted here as a result of kinetic effects during a process of magma crystallization and mixing. However, these features are not systematic that suggests a heterogeneous medium as discussed further. The sector zoning developed on the ~30 μm thick rim points to a final step of rapid crystallization with growth rates that could reach 10^{-6} cm/s or even faster (Kouchi et al., 1983). High growth rates are also in agreement with the amoeboid shape of ongoing crystallizing pyroxene (Fig. 4e) with composition $Fs_{10.7-13.7}$ (Mg# 0.81–0.76). The melt inclusion analyzed in this crystal shares a closely similar major element composition with the bulk lapilli (Gaua 27B; Table 1). In the majority of the analyzed crystals, rims reach composition Fs_{14-16} that also evidences a further and ultimate stage of crystallization.

In summary, the 2010 scoriae Gaua 27 and the lava Gaua 26 display the same chemical and mineralogical compositions, despite their textural difference in relation to their late stage cooling history. The chemical variability of the mineral phases is ascribed to repeated changes in the conditions of crystallization and in phase equilibria, because of combined processes of magma mixing, degassing and crystallization as discussed further.

4.3. Melt inclusions and matrix glasses

For melt inclusion study, we focused on the 2010 lapilli (~2–3 cm in size) which have been quenched when falling in the Lake Letas, and are characterized by a vesicle-rich, glassy matrix. We mainly focused on melt inclusions (MIs) in a set of clinopyroxene crystals whose compositions are representative of the entire pyroxene population which occurs in the 2009–2010 Garet samples (Table 2). Their common size is in the range ~70–20 μm. Parallelepiped shape MIs, which systematically display a large bubble of 15–20 μm in diameter and a spinel (i.e., CPX 22 in Fig. 4c), typify diopside. Systematic search of CO_2 and H_2O in the bubbles using μRaman was unsuccessful that indicates a very low density of gas. These MIs contrast with those in other clinopyroxene crystals formed by glass and one small bubble (i.e., CPX 21 in Fig. 4e) or no bubble at all. In plagioclase, fully enclosed MIs are numerous, commonly bubble-free and of small size (<50 μm), together with partially enclosed embayments. The dataset was thus complemented by the analyses of both MIs and embayments in plagioclase and of the glassy matrix.

Melt inclusions and embayments cover a significant range of chemical compositions for both major and volatile elements (Fig. 5), and plot in the fields of basaltic andesite and basaltic trachy-andesite.

MIs in Mg-rich clinopyroxene represent the less evolved end-member (MgO ~5.3 wt.%) with relatively low K_2O content (0.6–0.8 wt.%; $K_2O / Na_2O = 0.27–0.35$), as reported for the pre-1962 basalts of Mt Garet by Beaumais et al. (in this volume). They have the highest

Table 2
Representative compositions of melt inclusions and matrix glasses of the Mt Garet 2009–2010 products.

Sample	N[2]	SiO_2[3]	TiO_2	Al_2O_3	FeO_T[4]	MnO	MgO	CaO	Na_2O	K_2O	P_2O_5	H_2O	S	Cl	Total
Gaua 27A-Cpx21 MI	(3)	53.01	0.72	15.45	9.21	0.14	4.60	8.91	2.87	1.51	0.25	1.8	0.052	0.140	98.65
Gaua 27A-Cpx22 MIa	(3)	52.03	1.01	15.42	8.51	0.30	5.35	10.14	2.00	0.63	0.12	2.6	0.140	0.213	98.47
Gaua 27A-Cpx22 MIb	(2)	52.52	0.87	16.20	8.07	0.24	4.78	9.45	2.40	0.85	0.14	2.7	0.157	0.219	98.60
Gaua 27A-Cpx28 MI	(3)	50.53	0.88	16.41	9.13	0.28	5.29	10.64	2.41	0.66	0.15	1.7	0.153	0.194	98.43
Gaua 27A-Cpx26 MI	(2)	56.03	0.85	15.30	10.51	0.26	3.23	6.64	3.12	2.18	0.28	0.9	0.052	0.246	99.59
Gaua 27A-Cpx11 Emb.[1]	(4)	56.19	0.87	15.82	10.06	0.19	3.39	7.04	3.50	2.47	0.32	0.6	0.014	0.230	100.71
Gaua 27A-Cpx11 MI	(3)	55.12	0.79	15.22	10.26	0.23	3.58	6.99	3.77	2.23	0.28	1.0	0.051	0.247	99.76
Gaua 27A-Cpx23 MI	(3)	56.59	0.81	15.40	9.33	0.22	3.25	6.43	3.49	2.65	0.34	na	0.026	0.271	98.82
Gaua 27A-Pl4 Emb.	(2)	55.99	0.79	15.62	9.21	0.25	3.00	6.53	3.30	2.54	0.33	na	0.030	0.256	97.85
Gaua 27A-Pl4 Emb.	(3)	55.90	0.80	15.65	8.91	0.16	3.05	6.62	3.34	2.73	0.31	na	0.016	0.261	97.76
Gaua 27A-Pl3 Emb.	(5)	56.61	0.81	15.52	8.95	0.18	2.92	6.43	3.31	2.73	0.31	na	0.027	0.233	98.04
Gaua 27A-Pl49 MI	(2)	55.66	0.76	15.59	9.26	0.15	3.29	6.79	3.39	2.52	0.34	na	0.021	0.222	97.97
Gaua 27A-Matrix glass	(16)	55.97	0.82	15.48	9.88	0.21	3.41	6.82	3.59	2.45	0.31	na	0.030	0.249	99.23
	SD[5]	0.76	0.06	0.42	0.14	0.02	0.14	0.04	0.19	0.17	0.03		0.026	0.012	

na: not analyzed.
[1] Embayments correspond to open inclusions in contact with their surrounding.
[2] Number of averaged analyses.
[3] Concentrations of major oxides, H_2O, S, and Cl are given in wt.%.
[4] Fe expressed as total FeO.
[5] Standard deviation (in wt.%).

total volatile content (~3 wt.%) with 2.6–2.7 wt.% of H_2O, 0.14–0.16 wt.% of S, and 0.19–0.22 wt.% of Cl (S / Cl = 0.67–0.72).

Most MIs and embayments in both clinopyroxene and plagioclase have an evolved trachy-andesitic composition closely similar to that of the glassy matrix (K_2O = 2.3–2.7 wt.%; MgO 3.2–3.6 wt.%). They are strongly degassed and contain less than 0.05 wt.% of S, but display the highest dissolved amounts of Cl (0.26–0.29 wt.%). The H_2O content of clinopyroxene hosted MIs is less than 1 wt.%. Only a few MIs trapped in one single crystal (CPX25) recorded highly variable S content from 0.12 to 0.028 wt.%, whereas their H_2O (0.9–0.8 wt.%) concentrations are similar and Cl slightly increases (from 0.23 to 0.25 wt.%). This crystal displays resorption surface and contains micrometric Cu-bearing sulfides in association with secondary fluid inclusions that indicate its xenocrystic origin. More broadly sulfide globules have been observed neither as solid inclusions in the other mineral phases nor in the matrix despite a systematic search in the Gaua 26 lava block. Hence, we have considered that the segregation or the remobilization (external source) of sulfide globules did not significantly affect the global budget of sulfur at Mt Garet. This hypothesis is supported by the overall negative correlation between S and FeO (Fig. 5e).

Interesting is the occurrence of one MI with intermediate composition (K_2O = 1.5 wt.%; MgO = 4.6 wt.%) that nearly represents the 2010 magma of Mt Garet (Fig. 5a–c). This unique inclusion is trapped in a growing crystal (CPX21; Fig. 4e) and could be considered as a snapshot of the magma during its decompression and ascent. The total volatile content of 2 wt.% (1.8 wt.% of H_2O, 0.05 wt.% of S, and 0.14 wt.% of Cl) is also intermediate (Fig. 5d–f).

There is an overall negative correlation between H_2O and S that could be consistent with a process of magma mixing between melts having distinct volatile contents. However, such a process is not supported by the behavior of Cl (Fig. 5f), which alternatively suggests a major step of degassing as discussed further.

4.4. Optical thermometry measurements

The homogenization temperatures of melt inclusions hosted in plagioclase (a total of 18 measurements) range from 1087 to 1122 °C and average at 1108 ± 10 °C. The plagioclase — melt equilibrium was also computed using the geothermometers of Putirka (2008), for dissolved H_2O contents as measured in melt inclusions. We found equilibrium between the evolved trachy-andesitic glass (57 wt.% of SiO_2) containing 0.9, 0.6 and 0.2 wt.% of H_2O with plagioclase $An_{64.8–61.7}$ in the 1090–1112 °C temperature range. Hence there is a very good agreement between these latter calculations, optical thermometry measurements and plagioclase compositions.

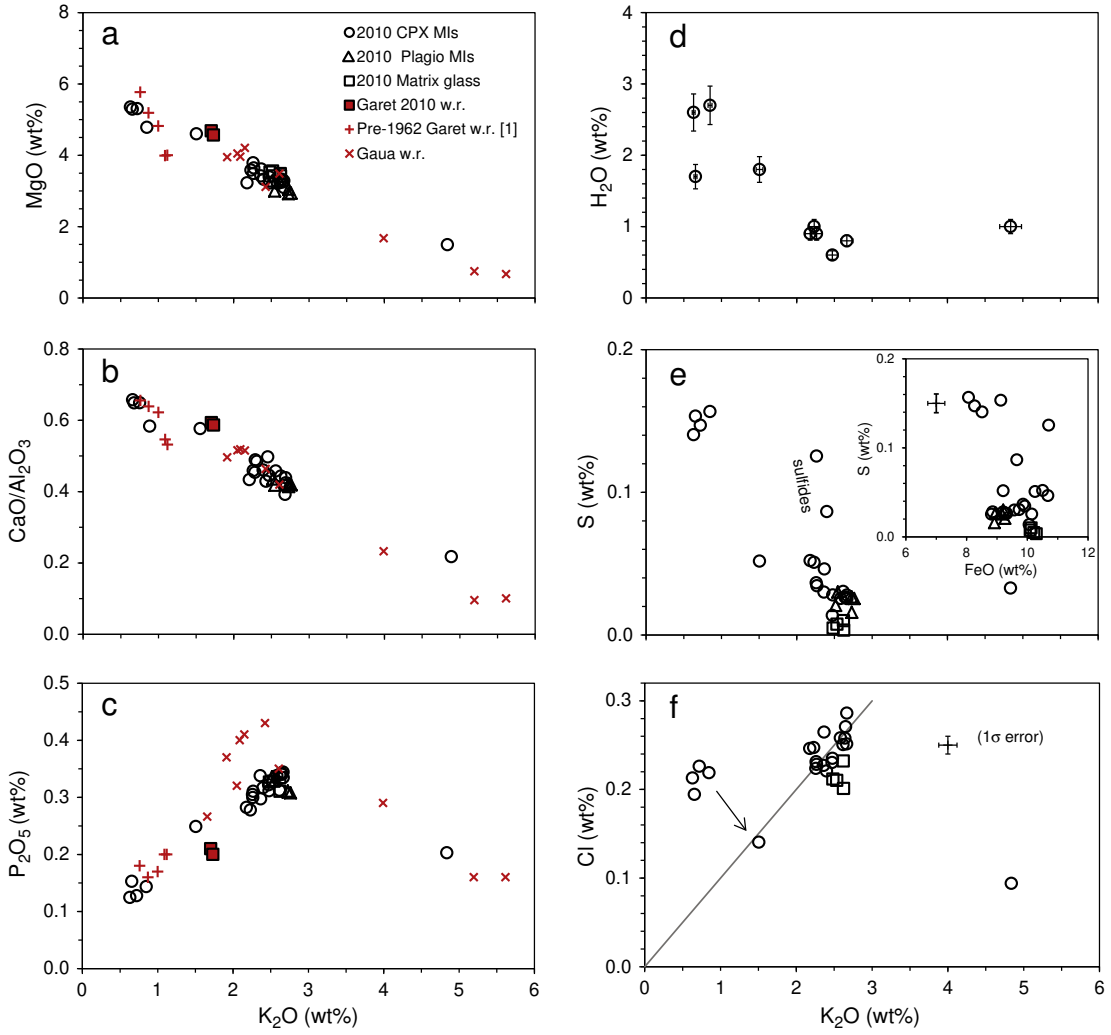

Fig. 5. Major and volatile compositions of melt inclusions (MIs) hosted in clinopyroxene and plagioclase and of the matrix glasses of the 2010 basaltic lapilli of Mt Garet. The insert in the plot e shows the respective evolution of S and FeO. In plot f the arrow indicates possible Cl exsolution during magma decompression and H_2O loss induced crystallization (see text). (Cl / K_2O) = [(0.83 × Cl / K)] in wt.

Table 3
Experimental viscosity measurements at low temperature.

T(K)	Log η (Pa s)
956.7	12.41
967.1	11.99
977.2	11.69
978.1	11.66
988.7	11.33
994.1	11.16
1010.1	10.70
1010.6	10.67
1019.6	10.42
1028.9	10.16
1030.6	10.13
1032.1	10.08
1051.8	9.60
1052.9	9.54
1067.5	9.28

4.5. Viscosity of the 2010 magma of Mt Garet

The experimental measurements of the viscosities in Gaua 26 anhydrous glass at low temperature are reported in Table 3. Viscosities, in the 1400–1700 K range, are calculated with Giordano et al. (2008) model. This latter provides good values at high temperature but is less accurate at low temperature as shown by the GKD points reported in the Fig. 6.

Viscosity measurements and calculated values for the anhydrous melt are fitted with the empirical Tammann–Vogel–Fulcher (TVF) equation:

$$\log\eta_o = A + B/(T - T_1) \quad (0)$$

A, B, and T_1 are adjustable parameters and T the temperature in Kelvin

From Le losq et al. (2015), we have assessed the viscosity values of a magma, which is a three phases mixture of melt with dissolved water, crystals and bubbles by summing different terms:

$$\mathrm{Log}\,\eta_{\mathrm{magma}} = \log\eta_{\mathrm{melt}} + X_{\mathrm{water}} + Y_{\mathrm{crystal}} + Z_{\mathrm{bubble}}. \quad (1)$$

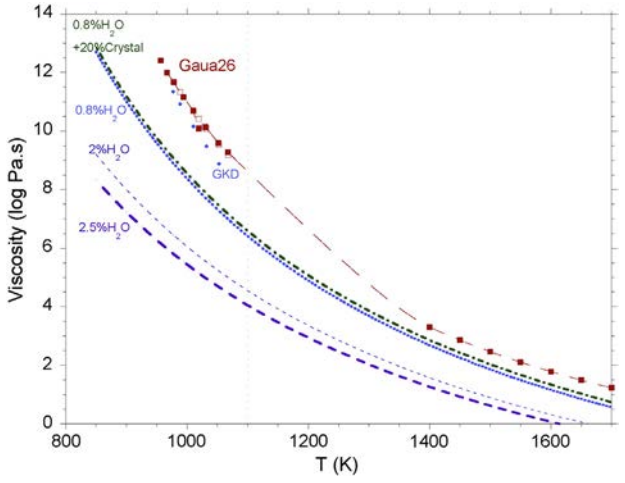

Fig. 6. Viscosity (log Pa s) as a function of the temperature (K) for the 2010 trachybasaltic andesite of Mt Garet (Gaua 26). The anhydrous sample curve (thick red curve) is obtained by using the Tammann–Vogel–Fulcher (TVF) equation fit of the laboratory experimental measurements at low temperature and the high temperature values calculated after Giordano et al. (2008). Variability at 1050 K is due to partial crystallization. The figure shows also the viscosity values (blue symbols, GDK) calculated at low temperature using Giordano et al. (2008) model. The other curves illustrate the change in magma viscosity as a function of the melt H_2O concentrations and crystal content (see text for explanation). (For interpretation of the references to color in this figure legend, the reader is referred to the web version of this article.)

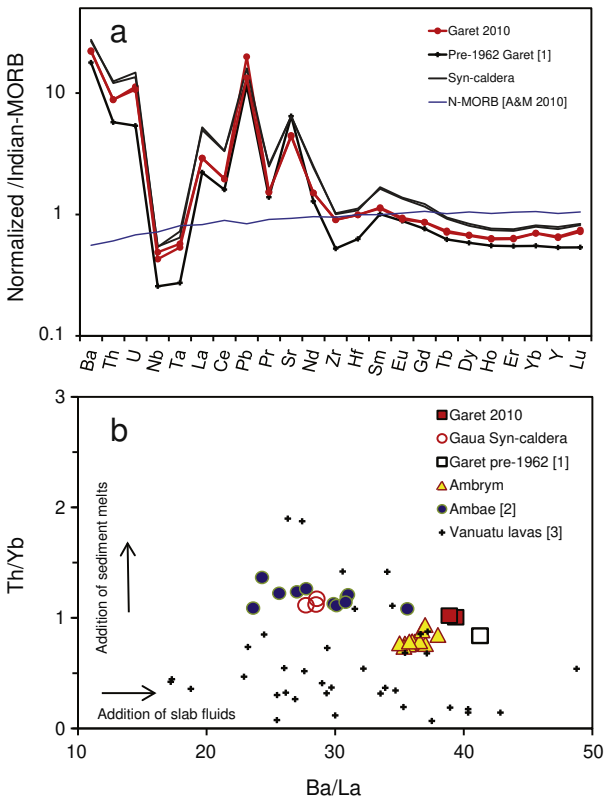

Fig. 7. a) Patterns of trace elements in bulk samples of the syn-caldera activity of Gaua volcano and of the pre-1962 and 2009–2010 activity of Mt Garet, normalized against Indian-MORB. Data for global N-MORB and Indian-MORB are from Arevalo and McDonough (2010). b) Variation of the Th/Yb and Ba/La in bulk rocks of caldera forming eruption of Gaua volcano and of the 2009–2010 eruption of Mt Garet, compared to lavas of the different segment of Vanuatu arc. Data are [1] from Beaumais et al. (in this volume; basalt SM52), [2] from Sorbadere et al. (2011), [3] from Peate et al. (1997) and Sorbadere et al. (2013b), and for Ambrym from Métrich and Bertagnini (unpub. data).

From Whittington et al. (2001) we can evaluate and add the water effect directly in the Eq. (0):

$$\log\eta_{H2O} = A + \left(B^{anh} + K_1 \times C_{H_2O} + K_2 \times C_{H_2O}{}^2\right) \div \left(T - \left(T_1{}^{anh} + K_3 \times C_{H_2O} + K_4 \times C_{H_2O}{}^2\right)\right) \quad (2)$$

with $K_1 = 455.52$, $K_2 = 32{,}626$, $K_3 = 110{,}61$, and $K_4 = 13{,}241$.

Finally, to take account of crystal proportion, we considered the equation given by Le Losq et al. (2015):

$$\log\eta_{\mathrm{magma}} = \log\left(\left[10^{\eta_{H2O}}\right] \times \left[1 - \Phi/\Phi_m\right]^{-2}\right) \quad (3)$$

where Φ is the volume fraction of crystals, and Φ_m is the maximum packing fraction of 0.52 (Lejeune and Richet, 1995; Le Losq et al., 2015).

At 1100 °C, the viscosity of Mt Garet anhydrous magma is $10^{3.5}$ Pa s. As expected adding 0.8 to 2.5 wt.% of H_2O results in the viscosity decrease by one to two orders of magnitude, respectively (Fig. 6). In contrast, the crystallization of 20 vol.% of minerals in a melt having 0.8 wt.% of H_2O leads to increase the viscosity of nearly 0.5 log unit. It implies at Mt Garet a significant contrast, of at least one order of magnitude, between the refilling and the partially degassed magmas.

Table 4
MELTS simulations of magma isobaric crystallization path.

Gaua 27 starting material	SiO_2[a]	TiO_2	Al_2O_3	Fe_2O_3	FeO	MgO	CaO	Na_2O	K_2O	P_2O_5	H_2O	CaO/Al_2O_3
Bulk rock	52.25	0.72	16.55	10.19	nd	4.57	9.70	3.14	1.73	0.20	−0.03	0.59
Glassy matrix	55.70	0.90	15.21	nd	10.21	3.48	6.97	3.57	2.56	0.33		0.46

MELTS simulations 1 — isobaric crystallization at 100 MPa, starting from Gaua 27 bulk rock composition with 1.7 wt.% of H_2O

T (°C)	Log fO_2	Mass (gm)	SiO_2[a]	TiO_2	Al_2O_3	Fe_2O_3	FeO	MgO	CaO	Na_2O	K_2O	P_2O_5	H_2O	CaO/Al_2O_3
Liquid 100 MPa 1.7 wt.% of H_2O														
1125	−8.46	100.0	52.18	0.72	16.53	2.10	7.27	4.56	9.69	3.14	1.73	0.20	1.70	0.59
1115	−8.59	96.4	52.28	0.73	16.95	2.09	7.31	4.20	9.24	3.25	1.79	0.21	1.76	0.55
1105	−8.72	93.1	52.39	0.73	17.35	2.09	7.33	3.85	8.81	3.35	1.86	0.21	1.82	0.51
1095	−8.85	90.1	52.51	0.73	17.73	2.08	7.34	3.53	8.39	3.46	1.92	0.22	1.88	0.47
1085	−8.98	86.2	52.70	0.75	17.78	2.11	7.47	3.31	7.88	3.57	2.00	0.23	1.97	0.44
Cpx 100 MPa 1.7 wt.% of H_2O												Wo[b]	Fs	Mg#
1115		3.6	49.54	0.52	5.25	2.98	5.55	14.37	21.60	0.19		45.0	13.4	0.757
1105		3.3	49.14	0.60	5.55	3.17	5.80	14.01	21.54	0.20		45.1	14.1	0.743
1095		3.0	48.73	0.68	5.85	3.36	6.06	13.64	21.47	0.22		45.2	14.9	0.728
1085		2.4	48.53	0.75	5.91	3.47	6.37	13.47	21.27	0.23		44.9	15.6	0.717
Plagio 100 MPa 1.7 wt.% of H_2O												An[b]		
1085		1.6	48.22		33.23				16.16	2.23	0.16	79.3		

MELTS simulations 2 — isobaric crystallization at 25 MPa, starting from Gaua 27 bulk rock composition with 1.0 wt.% of H_2O

T (°C)	Log fO_2	Mass (gm)	SiO_2[a]	TiO_2	Al_2O_3	Fe_2O_3	FeO	MgO	CaO	Na_2O	K_2O	P_2O_5	H_2O	CaO/Al_2O_3
Liquid 25 MPa 1.0 wt.% of H_2O														
1115	−8.60	87.4	53.09	0.79	16.40	2.31	7.84	4.18	8.49	3.43	1.98	0.23	1.04	0.52
1105	−8.73	82.7	53.30	0.82	16.38	2.36	8.05	3.95	7.92	3.55	2.09	0.24	1.10	0.48
1095	−8.86	78.5	53.50	0.85	16.36	2.40	8.25	3.73	7.40	3.67	2.19	0.26	1.16	0.45
1085	−9.00	71.9	54.95	0.76	16.48	2.18	7.28	3.39	6.87	3.89	2.39	0.28	1.26	0.42
Cpx 25 MPa 1.0 wt.% of H_2O												Wo[b]	Fs	Mg#
1115		3.2	49.55	0.50	5.07	3.15	6.06	14.43	21.04	0.21		43.8	14.5	0.743
1105		2.7	49.41	0.54	5.08	3.24	6.45	14.34	20.72	0.22		43.2	15.2	0.732
1095		2.3	49.28	0.59	5.08	3.32	6.88	14.27	20.36	0.23		42.5	16.1	0.720
1085		2.6	49.56	0.55	4.85	3.13	7.08	14.51	20.08	0.23		41.8	16.1	0.723
Plagio 25 MPa 1.0 wt.% of H_2O												An[b]		
1115		2.3	48.96		32.72				15.57	2.55	0.19	76.3		
1105		2.0	49.35		32.46				15.26	2.72	0.21	74.7		
1095		1.8	49.76		32.17				14.93	2.90	0.23	73.0		
1085		2.3	50.38		31.75				14.44	3.18	0.25	70.5		
Olivine 25 MPa 1.0 wt.% of H_2O												Fo[b]		
1085		0.03	38.05				23.77	36.98	0.39			73.3		
Spinel 25 MPa 1.0 wt.% of H_2O												Usp[b]		Fe^{2+}/Fe^{3+}
1095		3.1		6.39	6.64	51.64	30.09	5.23				0.171		0.648
1090		0.8		6.45	6.44	51.72	30.26	5.13				0.173		0.650
1085		0.7		6.51	6.23	51.79	30.46	5.02				0.175		0.654

MELTS simulations 3 — isobaric crystallization at 25 MPa, starting from simulations 2 at 1095 °C, with 0.8 wt.% of H_2O

T (°C)	Log fO_2	Mass (gm)	SiO_2[a]	TiO_2	Al_2O_3	Fe_2O_3	FeO	MgO	CaO	Na_2O	K_2O	P_2O_5	H_2O	CaO/Al_2O_3
Liquid 25 MPa 0.8 wt.% of H_2O														
1095	−8.86	91.6	54.09	0.92	15.72	2.54	8.72	3.52	6.89	3.78	2.38	0.29	0.87	0.44
1090	−8.93	84.7	55.84	0.79	15.88	2.21	7.33	3.26	6.59	3.99	2.56	0.31	0.94	0.42
1085	−9.00	81.3	56.51	0.76	15.86	2.12	6.92	3.09	6.37	4.08	2.66	0.32	0.98	0.40
Cpx 25 MPa 0.8 wt.% of H_2O												Wo[b]	Fs	Mg#
1095		1.2	49.32	0.57	4.86	3.38	7.65	14.30	19.67	0.24		41.1	17.4	0.704
1090		2.3	49.77	0.49	4.57	3.09	7.61	14.68	19.55	0.24		40.7	16.9	0.716
1085		1.0	49.87	0.48	4.47	3.03	7.73	14.74	19.44	0.25		40.4	17.0	0.715
Plagio 25 MPa 0.8 wt.% of H_2O												An[b]		
1095		6.3	51.00		31.32				13.94	3.43	0.30	68.0		
1090		2.1	51.54		30.96				13.52	3.67	0.32	65.8		
1085		1.5	51.89		30.72				13.23	3.82	0.34	64.4		
Olivine 25 MPa 0.8 wt.% of H_2O												Fo[b]		
1095		1.0		25.19			0.88	35.74	0.41			71.5		
1085		0.1		24.87			1.08	35.87	0.38			71.8		
Spinel 25 MPa 0.8 wt.% of H_2O												Usp[b]		Fe^{2+}/Fe^{3+}
1090		2.6		6.33	6.95	51.50	29.84	5.39				0.169		0.644
1085		0.7		6.38	6.74	51.58	30.02	5.28				0.170		0.647

[a] Chemical compositions are expressed in oxide wt.%.
[b] Amounts (in mol%) of Wo and Fs in clinopyroxene, An in plagioclase, Fo in olivine, and Usp in spinel.

5. Discussion

5.1. Gaua magma geochemistry and the 2010 eruption at Mt Garet

Syn-caldera trachybasalts display typical trace element patterns of arc-related magmas (Fig. 7a), with significant depletion in high field strength elements relative to the elements of similar incompatibility (Th / Ta = 21.8 ± 0.1) and also relative to N-MORB (Nb / Nb* = 0.75). Their Hf/Zr ratio (0.028) is typical of N-MORB (0.027; Arevalo and McDonough, 2010). They are relatively rich in Ba (Ba / La = 28.5 ± 1.2; Ba / Th = 185 ± 6) and alkalis (Rb / Th = 12.2 ± 0.9), as reported for magmas of the central part of the arc (e.g., Peate et al., 1997; Beaumais et al., in this volume).

Both the pre-1962 and the 2009–2010 basalts of Mt Garet belong to a new generation of basalts which differ from the pre- and syn-caldera trachy-andesites in being significantly depleted in incompatible elements. These features partly explain their relatively high Ba/La (41), decoupling between La and Ba in addition to preferential enrichment in fluid mobile elements as Ba (Fig. 7b). We stress here that the 2010 magma displays similar Sr concentrations and isotope ratio ($^{87}Sr / ^{86}Sr = 0.704027 \pm 6 \times 10^{-6}$) that the syn-caldera pyroclastites ($^{87}Sr / ^{86}Sr = 0.703978–0.704072$; Beaumais et al., in this volume). The significant enrichment in radiogenic Sr registered by the pre-1962 samples of Mt Garet could be likely related either to mantle processes as discussed by Beaumais et al. (in this volume) or to interactions between magma and altered crust, or country rock assimilation (e.g., Andrews et al., 2008), but this will require further study.

5.2. Magma migration, degassing, and crystallization

Mineral paragenesis made of clinopyroxene $Fs_{14–15}$, plagioclase $An_{64–62}$, olivine (Fo_{72}) and titanomagnetite coexists with diopsidic pyroxene $Fs_{5–9}$ and plagioclase $An_{86–78}$, whereas crystal outer rims achieve compositions of $Fs_{16–17}$ and An < 62, respectively. The occurrence of ongoing crystallizing microcrysts (Fig. 4e), which preserved the geochemical imprint of the 2010 erupted magma with a minimum H_2O concentration of ~1.8 wt.%, caught a unique feature. In contrast glass entrapped during the late stages of plagioclase and pyroxene crystallization are evolved (on average MgO = 3.3 ± 0.02 wt.%; CaO / Al_2O_3 = 0.44 ± 0.02) and closely comparable with respect to their major element chemistry to the residual glasses (Fig. 5a–c).

We computed the isobaric crystallization paths of the 2010 magma to fit as much as possible the mineral compositions, using MELTS (Ghiorso and Sack, 1995; Asimow and Ghiorso, 1998). Calculations are reported in Table 4. The oxygen fugacity is fixed at NNO buffer, arbitrarily. However, no sulfide globules were observed and the calculated (Fe^{2+}/Fe^{3+}) ratios of the spinels match those analyzed in the natural samples. The temperature interval brackets that of optical thermometry measurements. The range of H_2O concentrations from 1.7–1.8 to 0.8 wt.% used for calculations is based on the melt inclusion analysis, as at higher H_2O content there is no crystallization. We first started from a melt having the composition of the 2010 bulk rocks, a dissolved amount of H_2O of 1.7 wt.%, and a temperature range from 1125 down to 1085 °C. At 1125 °C and 100 MPa, there is no crystallization at all. Down to 1095 °C only clinopyroxene crystallizes ($Fs_{13.4–14.9}$), and plagioclase (An_{79}) appears at 1085 °C in very small amounts. Similar calculations at 50 MPa provide comparable results.

The mineral paragenesis of the 2010 products is better reproduced by two-step calculations and lower H_2O concentrations (simulations 2 and 3 in Table 4). In the first step, the starting material is still Gaua 27 bulk rock, the dissolved amount of H_2O is 1.0 wt.% and the calculations run down to 1095 °C. The computed mineral assemblage is mainly composed of clinopyroxene ($Fs_{14.5–16}$) and plagioclase ($An_{76–70}$), with subordinate Fe–Ti oxides (Fe^{2+} / Fe^{3+} = 0.65) which crystallize at 1095 °C. The extent of crystallization achieves 21.5 (wt) % and the residual melt contain 53.5 wt.% of SiO_2. The second step starts from this latter composition with 0.8 wt.% of H_2O that leads to the crystallization of plagioclase $An_{68–64}$, clinopyroxene (Fs ~17), Fe–Ti oxides (Fe^{2+} / Fe^{3+} = 0.64–0.65) and olivine (Fo ~72) in a minor amount (<1 wt.%). Plagioclase becomes the prevalent mineral phase (~10 wt.%), which results in a decrease of the wollastonite content of the coexisting clinopyroxene.

The imprint of more primitive magma prior to the 2010 eruption is clearly evidenced by crystallization of thin layers of high Mg# pyroxene and of sieved textured plagioclase as illustrated in Fig. 4. A few melt inclusions in diopsidic pyroxene indicate that this basalt–andesitic magma is (i) relatively K-poor, one of the geochemical characteristics that typifies both the pre-1962 and present-day magmas of Mt Garet compared to the syn-caldera pyroclastic series and the pre-caldera stage magmas, (ii) hydrated (possibly 2.7 wt.% of H_2O), and (iii) rich in both sulfur and chlorine (Fig. 5c). However, a simple process of fractional crystallization of a pre-1962 like, K-poor, magma batch is supported neither by the trace and major element data, since the concentrations of incompatible elements increase at nearly constant MgO content, nor by the mineral textures.

Combining all the chemical data on melt inclusions, minerals and bulk rocks, we propose that the 2009–2010 unrest at Mt Garet testifies the crystallization of hydrated and S, Cl-rich basalt batch(es) while degassing. Crystallization induced by water exsolution is contemporaneous to mixing between co-genetic melts which differed by their extents of crystallization and temperature. This hypothesis is supported by the existence of patchy zoned cores in plagioclase which are indicative of rapid crystallization events of skeletal crystals, followed by oscillatory zoning and dissolution surfaces.

The time for a 120 μm thick face to grow (i.e., clinopyroxene CPX 22; Fig. 4c) is estimated to be between 3 to 30 h for clinopyroxene growth rates of 10^{-7} to 10^{-8} cm/s (Dunbar et al., 1995). We stress that the time for crystal growth is only roughly estimated, because crystals are not well orientated, but is of the order of hours and days that means a short amount of time elapsed between magma crystallization, decompression and eruption at Mt Garet.

Finally, sector zoning on the pyroxene rims (i.e., Fig. 4d) implies high growth rates of the order of 10^{-6} cm s^{-1} or even less, according to Kouchi et al. (1983). These textural features are inferred to form while the decompression rate is accelerating just prior to eruption.

5.3. Degassing budget and implications

Bani et al. (2012, in this volume) have shown that the SO_2 flux strongly fluctuated in course of the Mt Garet eruptive crisis with peaks ≥3000 t d^{-1} in September and October 2009, and January and April 2010. These authors also derived the total amount of SO_2 (184 kt) released over 10 months of Mt Garet activity from space-borne Ozone Monitoring Instrument (OMI) data. Although it is considered as a minimum because of the limitations of OMI data treatment and interpretation as discussed by Bani et al. (in this volume) we considered this value of 184 kt to quantify the magma volume which is required to sustain the atmospheric SO_2 burden. In the same period of time, 72 kt of Cl were also released, while negligible quantities of juvenile magma were erupted.

Assuming that the total mass of sulfur released during the 2009–2010 unrest was sustained by the basaltic magma batches which refilled the system we may estimate the volume of un-erupted magma as typically done on the basis of melt inclusions and degassed melt prior to eruption glasses following the equation:

$$M_i = \left[C_0^i - \left(C_{deg}^i \times f\right)\right] \times M_{magma} \quad (4)$$

Mi is the mass of the element i (S or Cl) released into the gas phase; C_0^i and C_{deg}^i the concentrations of the element before and after degassing, respectively; f (0.28) the fraction of residual melt is derived from the K_2O_0/K_2O_{deg} ratio (where K_2O_0 is the concentration of the

MIs representative of the basaltic magma before degassing) and M_{magma} the mass of magma. The initial amounts of dissolved S and Cl in the basaltic MIs, average at 1480 ± 81 ppm and 2185 ± 53 ppm, respectively. They are typical of arc basaltic andesites (e.g., Wallace and Edmonds, 2011; Longpré et al., 2014). The residual volatile content is derived from the degassed MIs in plagioclase and clinopyroxene. It averages at 256 ± 60 ppm for S and 2457 ± 180 ppm for Cl. The proportion of chlorine exsolved into the gas phase achieves 69% against 95% for S. These latter proportions are observed at many volcanoes, even though Cl degassing from basaltic magmas strongly depends on the eruption dynamics, and they reflect the fact that Cl is more soluble in basaltic melt than S at low pressure (for a review see Métrich and Wallace, 2008). The density of the melt with 2.7 wt.% of H_2O is calculated to be 2.44 g.cm^{-3}, following Lange and Carmichael (1990).

From the Eq. (4), the computed magma volume required to produce a total mass of 184 kt of SO_2 is 0.027 km^3 that is a minimum, while 72 kt of Cl would have derived from 0.020 km^3 of magma. There is a relatively good convergence between the volume estimates deduced from SO_2 and Cl in gas emissions. Hence, the dominant source of S and Cl would be the refilling basalt akin to the pre-1962 basaltic lavas of Mt Garet.

Volatile degassing could be a non-linear process and operate as a multi-step degassing process. Fig. 5f illustrates the marked decrease of the dissolved amount of Cl contemporaneously to H_2O release and basaltic magma evolution towards compositions akin to the basaltic trachy-andesite erupted in 2010. This behavior cannot be explained by Cl diffusion during magma ascent and cooling because the melt inclusion was partly opened and exchanged with the surrounding magma. In addition, the positive correlation between P_2O_5 and K_2O ruled out not only significant Cl sequestration by apatite, but also diffusion effect due to rapid rates of crystal growth as phosphorus has a low diffusivity (Baker, 2008). It reveals Cl fractionation into the H_2O-rich gas phase with a calculated repartition coefficient $D_{Cl}^{fluid/melt}$ of 2.2. In contrast the second step is dominated by magma crystallization at constant Cl/K ratio (0.12 ± 0.01), while less than 10% could have degassed at time of eruption. If true magma, decompression would provide a large quantity of volatiles dominated by H_2O (~88%) and most likely CO_2 with S/Cl wt ratio nearly equal to the unit. Actually, increasing fluxes of S and Cl at Mt Garet tracks shallow magma and gas refilling.

5.4. A potential scenario for the 2009–2010 eruption of Mt Garet

We propose, here, a qualitative scenario (Fig. 8) for the eruptive processes reported at Mt Garet to explain as much as possible the chemistry of bulk rocks and minerals and the presently known 2009–2010

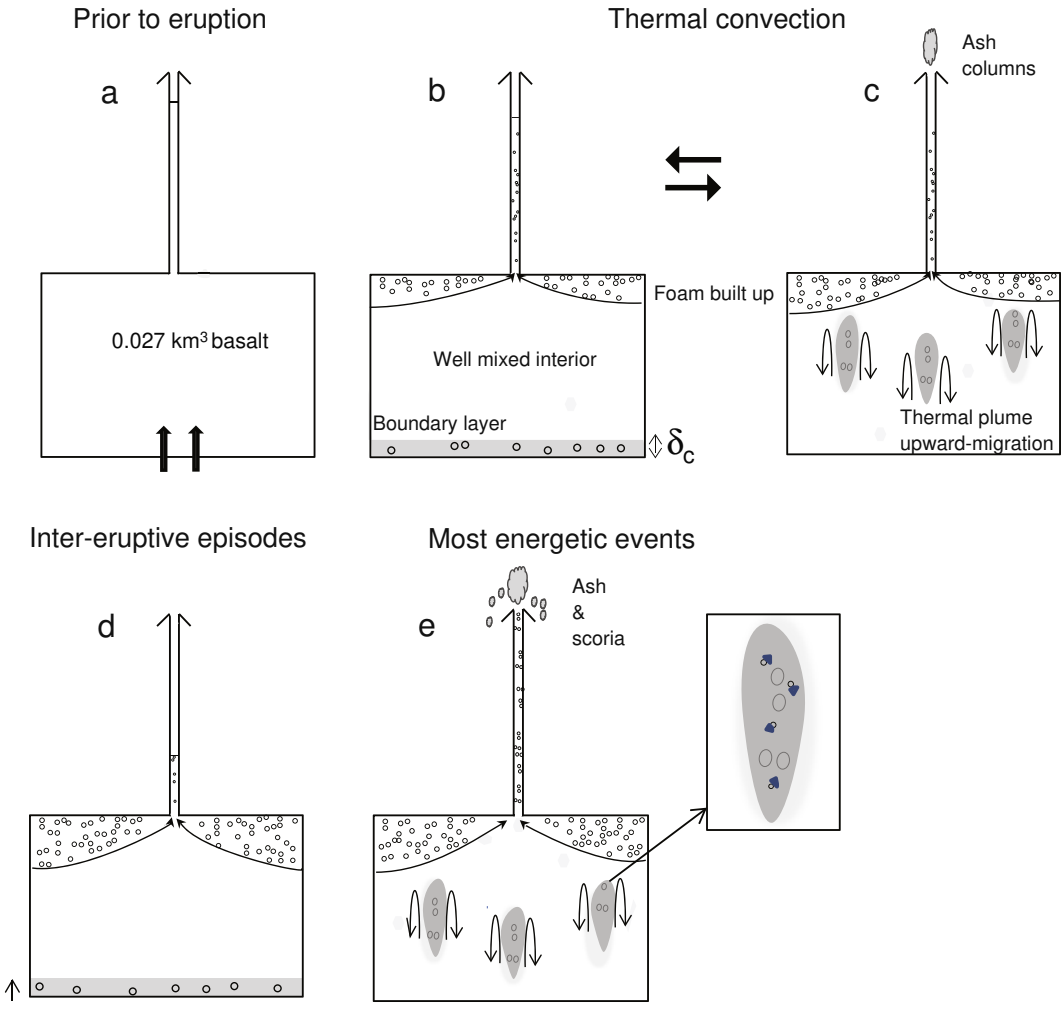

Fig. 8. Schematic representation (not to scale) of the possible scenario of the Mt Garet unrest. a. Emplacement of a basaltic magma batch, with possibly CO_2-rich bubbles, within the two years that preceded the surface manifestations; b. Convective cycles involving the development of a bottom boundary layer of bubbly magma which is crystallizing and degassing, and the progressive built up of a foam at the top of the reservoir where crystallization also proceeds; c. When the critical thickness (δ_c) of the bottom layer is reached, upward-migration of thermal plumes, which is a three-phase mixture, with aggregation of more homogeneous, slightly colder, H_2O-rich basaltic magma parcels existing in the well-mixed interior, crystal resorption/chemical and oscillatory zoning, and foam spreading into the conduit ultimately responsible for sustaining ash columns; d. Establishment of a stable level in the magma column due to a stable foam at the top of the reservoir and newly forming bubbles within the growing bottom boundary layer; e. Upward-motion of possibly bubbly magma blobs contained in the thermal plumes, and bubble nucleation enhanced by significant amount of titanomagnetite, trigger the most violent eruptive phases at Mt Garet. We stress that the well-mixed interior is not infinite.

eruptive activity. The number of samples which have been studied is limited. However from the present knowledge the 2009–2010 crisis was a "discrete" event in the sense that it took place within ≤3 years, after a long period of rest. It is thus highly important to try to better constrain the physical conditions of magma ascent and degassing at Mt Garet.

5.4.1. Convection and bubbly thermal plumes

Firstly, the unrest that initiated possibly within the two years that preceded the 2009–2010 event, when the vegetation covering Mt Garet cone started to decline, would require increase of temperature and fumarolic activity, and thus time for a deeper-derived primitive magma transfer through the crust, crystallization and production of a more evolved basalt equivalent to pre-1962 basalt Mt Garet (diopside hosted basaltic MIs). The ascent of such basaltic batch, towards its injection at the depth of a shallow reservoir is likely to have produced both a pressure source inside the edifice, favorable to development of small cracks, and an additional heat source. It is interesting to consider that, for a cylindrical shape reservoir, 0.027 km^3 would correspond to the volume of a cylinder of ~150 m radius and 400 m height. This magma volume cannot be stored within the cone itself.

The existence of a significant SO_2 flux, as measured early October 2009 (35 ± 12 kg s^{-1}; Bani et al., 2012), suggests that bubbles may have reached the surface via cracks from the top of the magma reservoir or directly via the conduit. In a basaltic system, sulfur may be exsolved into the gas phase as pressure decreases from 100 to 25 MPa or lower (e.g., Lesne et al., 2011). Sulfur exsolution occurs as soon as the magma reached a depth of 3.6–3.7 km or less, if at equilibrium, and even before it may eventually pond at the structural discontinuity between the volcanic edifice and the ocean floor at 2.4 km depth.

Secondly, basalt emplacement at shallow level (Fig. 8a) may have resulted from a series of pulses or from a unique event of progressive re-injection. Emplacing a magma volume of ~0.027 km^3 in the volcanic edifice does not necessarily require an incremental growth. This would have progressively decreased the effect of the new magma on the sequence of crystallization that is not supported by the mineralogy of the few studied samples. Although to be confirmed, we favor the hypothesis of one single event of magma arrival, in agreement with the main features of whole eruptive period.

Third, changes in the $T-P_{H_2O}$ conditions of magma crystallization recorded through mineral oscillatory zoning and resorption surfaces can be explained by a convective mechanism of magma blob transport to the top of the magma reservoir. Several types of convection are possible but they all require the existence of thin boundary layers, which pass through cycles of growth and dismantlement (Worster et al., 1990, 1993; Jaupart and Tait, 1995; Jellinek and Kerr, 2001). In the simplest case of thermal convection, the bottom boundary layer, in which the crystals are mostly growing, is unstable due to the release of latent heat associated to crystallization while the top boundary layer is stable. In a typical well-developed convective cycle, the bottom boundary layer thickens simultaneously to crystal nucleation and growth, while the temperature is the same in the largest part of the magma reservoir, called the well-mixed interior (Fig. 8b). When the bottom boundary layer exceeds its critical thickness (δ_c), it is no longer stable, and is dismantled into a horizontal series of thermal plumes which rise upwards. The thermal plumes are rich in a gas exsolved phase (bubbly plume) if the basaltic magma that is emplaced at the onset of the unrest contains pre-existing CO_2 bubbles or/and bubble formed in the boundary layer. While coming upward, they aggregate well-mixed magma blobs by advection (Fig. 8c). The well-mixed interior (with constant density and temperature) corresponds to the H_2O-rich, less differentiated basalt that can be colder compared to the thermal plumes which migrate upward because of the latent heat of crystallization. If true there is competition between the effect of temperature and the influence of H_2O on the phase stability. Phase equilibrium calculations, using MELTS (Ghiorso and Sack, 1995; Asimow and Ghiorso, 1998) at constant $T-P_{H_2O}$ (50 MPa) and temperature (1105 °C), show, that Mt Garet magma will contain 4 wt.% clinopyroxene crystals for a dissolved amount of H_2O of 1.7 wt.%. The extent of crystallization severely increases up to 21 wt.% when the H_2O concentration reaches ≤1.0 wt.%, while plagioclase and clinopyroxene crystallize in the same proportions. Hence this latter mineral paragenesis will not be longer stable in the water-rich melt.

However, we stress that crystallization in the bottom boundary layer is isobaric that will enhance CO_2 exsolution while the melt becomes enriched in H_2O at fluid saturation. If the melt is not saturated, the dissolved amounts of both CO_2 and H_2O will increase. Temperature and water increase will have an opposite effect on the melt viscosity that should not significantly change. More importantly it implies that major H_2O and S degassing will not take place there but most likely during the blob transfer towards the top of the reservoir.

5.4.2. Foam build up and system pressurization

The eruption is marked by a much larger quantity of expelled gas compared to magma, implying the presence of an exsolved gas phase at depth, which is accumulating at the top of the reservoir.

Bubbles formed in the boundary layer, if small enough, can be passively carried away by the bubbly thermal plumes, much faster than if they were rising with their Stokes velocity typical of isolated bubbles (Cardoso and Woods, 1999). They progressively accumulate to the top of the reservoir forming a foam, they increase the gas volume and pressurize the plumbing system. A mechanism based on a bubbly thermal convection with small and stagnant bubbles (0.3 mm) is proposed to account for by the 5-day cycles at the nearby basaltic active volcanoes of Ambrym Island (Vanuatu) (Vergniolle et al., in preparation). The 10-day cycles observed at Erta Ale (Ethiopia) were explained by a bubbly thermal boundary layer but with bubbles sufficiently large (0.4–0.6 mm) to escape the thermal boundary layer prior to its detachment (Vergniolle and Bouche, in revision).

The foam spreading leads to a small gas flux in the conduit (Jaupart and Vergniolle, 1988; Vergniolle and Jaupart, 1990). The observed activity (i.e., ash column) at Mt Garet suggests that the growing foam at the top of the reservoir is stable with respect of bubble coalescence. In contrast, massive foam coalescence (unstable foam) would have produced strong Strombolian activity or high-level lava fountains as demonstrated by laboratory experiments (Jaupart and Vergniolle, 1988; Vergniolle and Jaupart, 1990).

An eruptive event (i.e. ash column) can result from the accumulation of a relatively large gas volume, i.e. in the bubbly magma reservoir, in the foam at the top of the reservoir or in the conduit, which is suddenly released at the surface (Fig. 8c).

Once the eruptive column has stopped and the level of the magma in the conduit has dropped, the magma column could be stagnant for a time sufficiently long to be overlain by solid crust at the surface (Fig. 8d). Water loss at one atmosphere is an efficient mechanism to form a thin crust, especially since the extent of crystallization but also the melt viscosity drastically increases. In Mt Garet magma, when the H_2O amount dissolved in the melt declines from 2.5 to <0.1 wt.% the melt viscosity increases by 2 log units, from $10^{1.5}$ to $10^{3.5}$ Pa s, at 1100 °C (1373 K in Fig. 6), in agreement with previous measurements of andesitic melt viscosity (e.g., Richet et al., 1996; Vetere et al., 2006).

A constant level of the magma in the conduit is best achieved at the end of a convective cycle and during the growth of the bottom thermal boundary layer, in which the stagnant bubbles do not grow by decompression. Meanwhile, the bottom boundary layer thickens until becoming unstable to produce thermal plumes and its stagnant small bubbles, leading to another small increase in the gas volume. Therefore each cycle of the bubbly-thermal convection increases the gas volume trapped in the reservoir until a critical threshold in pressure is reached. At that time the cap formed at the surface, because of magma cooling

between explosive events (i.e. eruptive columns), is broken and the bubbles accumulated in the conduit are released at the surface to form an ash column.

5.4.3. A possible additional role of the titanomagnetite

Bubble nucleation requires the melt to be gas supersaturated in the absence of crystals or with crystals having a low wetting angle between the crystal-liquid interface and the bubble-liquid interface with, as an example, a ΔP of 10–30 MPa for H_2O-bubbles with most crystals such as pyroxene, plagioclase, and olivine (Lensky et al., 2006). In contrast, magnetite enhances bubble nucleation because of its very high wetting angle, making bubble nucleation occurring almost at equilibrium with the exsolution law (Hurwitz and Navon, 1994; Mourtada-Bonnefoi and Laporte, 2002; Gardner and Denis, 2004; Cluzel et al., 2008).

The scoria samples expelled during the most violent events early 2010 (i.e., mild Strombolian activity) contain titanomagnetite microcrysts that coexist with plagioclase, pyroxene and scarce olivine. MELTS calculations indicate that Fe–Ti oxides crystallize at 1095–1090 °C in small but significant proportions (2.5–2.0 wt.%; 0.5–0.4 vol.%). Bubble nucleation initiated on titanomagnetite crystals is an efficient mechanism to increase the volume of the bubbly magma in the reservoir (Fig. 8e). Once the nucleation is triggered, it can be very fast (Gardner, 2012). Increasing proportions of titanomagnetite and thus gas volume is a possible mechanism to trigger gas release within a series of (~3 km-high) eruptive columns within a week (in January 27–February 4, 2010).

Following this line of reasoning, the few hours required to form the last growing steps of clinopyroxene phenocrysts, as discussed above, would correspond to the time of magma transfer from its ponding zone to surface. Similar timing for magma decompression and ascent has been proposed at other volcanoes such as, for example, Stromboli (Métrich et al., 2005), or Fuego (Lloyd et al., 2014).

After February 2010, the intensity of the eruptive events declined, as did the pressure and the gas volume in the magma reservoir, before the unrest was over. Magma depletion in dissolved volatiles progressively weakened its ability to nucleate bubbles.

6. Conclusions

We provide here evidence of Garet system refilling by a basaltic magma batch (i) which belongs to a new generation of basalts and differs from the pre- and syn-caldera trachy-andesites in having relatively low concentrations in alkalis (K, Rb, Cs) and incompatible elements (i.e., Th, La, Nb), but higher Rb/Th ratios, and (ii) which is thought to be the source of sulfur and chlorine released in the atmosphere during the 2009–2010 unrest. The un-erupted basaltic magma dominates in volume. Crystal textures reveal (i) high undercooling episodes most likely associated with decompression events; (ii) pyroxene growth rates that could be faster than of 10^{-6} cm/s to account for by the sector zoning (Kouchi et al., 1983) which characterize the final stage of clinopyroxene crystallization; but also (iii) a short span of time, of the order of hours or a few tens of hours, for magma ascent.

We propose tentatively a model for the 2009–2010 period of unrest at Mt Garet that would imply the development of thermal convection with an unstable bottom boundary layer that dismantles, while reaching a critical thickness, and generates thermal plumes, possibly bubbly thermal plumes, which migrate upwards. Bubble accumulation at the top of magma reservoir concurs to the development of a foam which spreads in the conduit and, together with the significant amount of small bubbles, produces ash-columns. The additional effect of titanomagnetite, strongly enhancing bubble nucleation, is a possible mechanism that triggered the series of the most violent explosive events (i.e., mild strombolian activity) early 2010.

Mt Garet is one of the active volcanoes of the Vanuatu arc Central block, as open-conduit basaltic volcanoes (Marum and Benbow) on Ambrym Island and Lopevi which has been intermittently active with ash columns, lava flows, and subplinian eruptions (e.g., Warden, 1967; Beaumais et al. 2013). It differs from the others by the frequency of its eruptions and eruptive styles. Hence, a better knowledge of the chemistry and mineralogy of Mt Garet cone and of its eruptive activity is required to better understand the short-term unrest of this volcano, but also the volcanic activity in this part of the arc with respect to their geodynamic context.

Supplementary data to this article can be found online at http://dx.doi.org/10.1016/j.jvolgeores.2015.06.003.

Funding

This work was supported by the ANR contract ANR-06-CATT-02 Arc-Vanuatu and CNRS-INSU, 2010 ALEA CT3 programs. This is IPGP contribution 3616.

Acknowledgments

We are grateful to G. Jolly for having collected the lapilli on the Lake Letas in February 2010. We thank two anonymous reviewers for their useful remarks, P. Floury for his analytical work in the framework of his Master 1 (IPGP), S. Hidalgo (IPGP) for her help in sample preparation, and P. Pantani (INGV) for her graphical assistance. Our fieldwork benefited from kind local supports on Gaua, and we are grateful to the chief of Ontar village.

References

Andrews, B.J., Gardner, J.E., Housh, T.B., 2008. Repeated recharge, assimilation, and hybridization in magmas erupted from El Chichón as recorded by plagioclase and amphibole phenocrysts. J. Volcanol. Geotherm. Res. 175, 415–426.

Arevalo Jr., R., McDonough, D.W., 2010. Chemical variations and regional diversity observed in MORB. Chem. Geol. 271, 70–85. http://dx.doi.org/10.1016/j.chemgeo.2009.12.013.

Asimow, P.D., Ghiorso, M.S., 1998. Algorithmic modifications extending MELTS to calculate subsolidus phase relations. Am. Mineral. 83, 1127–1132.

Aubert de la Rüe, E., 1960. Les manifestations actuelles du volcanisme aux Nouvelles Hébrides (Mélanésie). Bull. Volcanol. 23, 197–205.

Baillard, C., Crawford, W.C., Ballu, V., Regnier, M.M., Pelletier, B., Garaebiti, E., 2013. Seismicity and geodynamics in the central part of Vanuatu arc. AGU Fall Meeting, 2013, San Francisco, T23H06B.

Baker, D.R., 2008. The fidelity of melt inclusions as records of melt composition. Contrib. Mineral. Petrol. http://dx.doi.org/10.1007/s00410-008-0291-3.

Bani, P., Oppenheimer, C., Allard, P., Shinohara, H., Tsanev, V., Carn, S., Lardy, M., Garaebiti, E., 2012. First estimate of volcanic SO_2 budget for Vanuatu island arc. J. Volcanol. Geotherm. Res. 211–212, 36–40.

Bani, P., Shinohara, H., Boudon, G., Balcone-Boissard, H., Delmelle, P., Quiniou, T. Lefèvre, J., Garaebiti, E., Shinohara, H., and Lardy, M., (in this volume). The 2009–2010 eruption of Gaua volcano (Vanuatu archipelago): eruptive dynamics and unsuspected strong halogen source. J. Volcanol. Geotherm. Res., (under review).

Beaumais, A., Chazot, G., Dosso, L., Bertrand, H., 2013. Temporal source evolution and crustal contamination at Lopevi Volcano, Vanuatu Island Arc. J. Volcanol. Geotherm. Res. 26, 72–84. http://dx.doi.org/10.1016/j.jvolgeores.2013.07.005.

Beaumais, A., Bertrand, H., Chazot, G., Dosso, L., Robin, C. (in this volume). Temporal magma source evolution at Gaua Volcano, Vanuatu Island Arc. J. Volcanol. Geotherm. Res. (under review).

Bulletin of the Global Volcanism Network (2009) volume 34/10, 11, 12. Smithsonian Institution Global Volcanism Program.

Bulletin of the Global Volcanism Network (2010) volume 35/5. Smithsonian Institution Global Volcanism Program.

Calmant, S., Pelletier, B., Lebellegard, P., Bevis, M., Taylor, F.W., Phillips, D.A., 2003. New insights on the tectonics along the New Hebrides subduction zone based on GPS results. J. Geophys. Res. 108/B6, 2319–2339.

Cardoso, S.S.S., Woods, A.W., 1999. On convection in a volatile-saturated magma. Earth Planet. Sci. Lett. 168, 301–310.

Cluzel, N., Laporte, D., Provost, A., Kannewischer, I., 2008. Kinetics of heterogeneous bubble nucleation in rhyolitic melts: implications for the number density of bubbles in volcanic conduits and for pumice textures. Contrib. Mineral. Petrol. 156, 745–763.

Collot, J.Y., Daniel, J., Burne, R.V., 1985. Recent tectonics associated with the subduction/collision of the d'Entrecasteaux zone in the Central New Hebrides. Tectonophysics 112, 325–356.

Davidson, J.P., Morgan, D.J., Charlier, B.L.A., Harlou, R., Hora, J.M., 2007. Microsampling and isotopic analysis of igneous rocks: implications for the study of magmatic systems. Annu. Rev. Earth Planet. Sci. 35, 273–311.

Dunbar, N.W., Jacobs, G.K., Nenay, M.T., 1995. Crystallization processes in an artificial magma: variations in crystal shape, growth rate and composition with melt cooling history. Contrib. Mineral. Petrol. 120, 412–425.

Gardner, J.E., 2012. Surface tension and bubble nucleation in phonolite magmas. Geochim. Cosmochim. Acta 76, 93–102.

Gardner, J.E., Denis, M.H., 2004. Heterogeneous bubble nucleation on Fe–Ti oxide crystals in high-silica rhyolitic melts. Geochim. Cosmochim. Acta 68, 3587–3597.
Ghiorso, M.S., Sack, R.O., 1995. Chemical transfer in magmatic processes IV. A revised and internally consistent thermodynamic model for the interpolation and extrapolation of liquid–solid equilibria in magmatic system at elevated temperatures and pressures. Contrib. Mineral. Petrol. 119, 197–212.
Ginibre, C., Kronz, A., Wörner, G., 2002. High-resolution quantitative imaging of plagioclase composition using accumulated backscattered electron images: new constraints on oscillatory zoning. Contrib. Mineral. Petrol. 142, 436–448.
Ginibre, C., Wörner, G., Kronz, A., 2007. Crystal zoning as an archive for magma evolution. Elements 3, 261–266.
Giordano, D., Russell, J., Dingwell, D., 2008. Viscosity of magmatic liquids: a model. Earth Planet. Sci. Lett. 271, 123–134.
Humphreys, M.C.S., Blundy, J.D., Sparks, R.S.J., 2006. Magma evolution and open-system processes at Shiveluch volcano: insights from phenocrysts zoning. J. Petrol. 47, 2303–2334. http://dx.doi.org/10.1093/petrology/egl045.
Hurwitz, S., Navon, 0., 1994. Bubble nucleation in rhyolitic melts — experiments at high-pressure, temperature, and water-content. Earth Planet. Sci. Lett. 122, 267–280.
Jaupart, C., Tait, S., 1995. Dynamics of differentiation in magma reservoirs. J. Geophys. Res. 100/B9, 17615–17636.
Jaupart, C., Vergniolle, S., 1988. Laboratory models of Hawaiian and Strombolian eruptions. Nature 331, 58–60.
Jellinek, A.M., Kerr, R.C., 2001. Magma dynamics, crystallization, and chemical differentiation of the 1959 Kilauea Iki lava lake, Hawaii, revisited. J. Volcanol. Geotherm. Res. 110, 235–263.
Jenner, F.E., O'Neill, H.St.C., 2012. Major and trace analysis of basaltic glasses by laser-ablation ICP-MS. Geochem. Geophys. Geosyst. 13 (3). http://dx.doi.org/10.1029/2011GC003890.
Joron, J.L., Treuil, M., Raimbault, L., 1997. Activation analysis as a geochemical tool: statement of its capabilities for geochemical trace element studies. J. Radioanal. Nucl. Chem. 216, 229–235.
Kouchi, A., Sugawara, Y., Kashima, K., Sunagawa, I., 1983. Laboratory growth of sector zoned clinopyroxenes in the system $CaMgSi_2O_6$–$CaTiAl_2O_6$. Contrib. Mineral. Petrol. 83, 177–184.
Landi, P., Métrich, N., Bertagnini, A., Rosi, M., 2004. Dynamics of magma mixing and degassing recorded in plagioclase at Stromboli (Aeolian Archipelago, Italy). Contrib. Mineral. Petrol. 147, 213–237.
Lange, R., Carmichael, I.S.E., 1990. Thermodynamics properties of silicate liquids with emphasis on density, thermal expansion and compressibility. In: Nicholls, J., Russel, J.K. (Eds.), Understanding Magmatic Processes. Modern Methods of Igneous Petrology. Reviews in Mineralogy 24, pp. 25–64.
Le Losq, C., Neuville, D., Moretti, R., Roux, J., 2012. Determination of water content in silicate glasses using Raman spectrometry: implications for the study of explosive volcanism. Am. Mineral. 97, 779–790.
Le Losq, C., Neuville, D., Moretti, R., Kyle, P.R., Oppenheimer, C., 2015. Rheology of phonolitic magmas — the case of the Erebus lava lake. Earth Planet. Sci. Lett. 411, 53–61.
Lensky, N.G., Niebo, R.W., Lyakhovsky, J.R., Holloway, V., Navon, O., 2006. Bubble nucleation as a trigger for xenolith entrapment in mantle melts. Earth Planet. Sci. Lett. 245, 278–288.
Lesne, P., Kohn, S., Blundy, J., Witham, F., Botcharnikov, R.E., Behrens, H., 2011. Experimental simulation of closed-system degassing in the system basalt-H_2O-CO_2-S-Cl. J. Petrol. 52, 1737–1762. http://dx.doi.org/10.1093/petrology/egr027.
Lloyd, A.S., Ruprecht, P., Hauri, E.H., Rose, W., Gonnermann, H.M., Plank, T., 2014. NanoSIMS results from olivine-hosted melt embayments: magma ascent rate during explosive basaltic eruptions. J. Volcanol. Geotherm. Res. 283, 1–18.
Longpré, M.-A., Stix, J., Burkert, C., Hansteen, T. Kutterolf S., 2014. Sulfur budget and global climate impact of the A.D. 1835 eruption of Cosigüina volcano, Nicaragua. Geophys. Res. Lett. http://dx.doi.org/10.1002/2014GL061205.
Mallick, D.I.J., Ash, R.P., 1975. Geology of the Southern Banks Islands. New Hebrides Condominium Geological Survey, Reportpp. 1–33.
Meffre, S., Crawford, A.J., 2001. Collision tectonics in the New Hebrides arc (Vanuatu). Island Arc 10, 33–50.
Mercier, M., et al., 2009. Influence of glass polymerisation and oxidation on microRaman water analysis in alumino-silicate glasses. Geochim. Cosmochim. Acta 73, 197–217. http://dx.doi.org/10.1016/j.gca.2008.09.030.
Métrich, N., Wallace, P., 2008. Volatile abundances in basaltic magmas and their degassing paths tracked by melt inclusions. In: Putirka, K., Tepley, F. (Eds.), Minerals, Inclusions & Volcanic Processes. Rev. Mineral. Geochem. 69, Chapter 10, pp. 363–402.
Métrich, N., Deloule, E., 2014. Water content, δD and $\delta^{11}B$ tracking in the Vanuatu arc magmas (Aoba island): insights from olivine-hosted melt inclusions. Lithos 206–207, 400–408. http://dx.doi.org/10.1016/j.lithos.2014.08.011.
Métrich, N., Bertagnini, A., Landi, P., Rosi, M., Belhadj, O., 2005. Triggering mechanism at the origin of paroxysms at Stromboli (Aeolian archipelago, Italy): the 5 April 2003 eruption. Geophys. Res. Lett. 32, L103056. http://dx.doi.org/10.1029/2004GL022257.
Mourtada-Bonnefoi, C.C., Laporte, D., 2002. Homogeneous bubble nucleation in rhyolitic magmas: an experimental study of the effect of H_2O and CO_2. J. Geophys. Res. 107/B4, 1–19. http://dx.doi.org/10.1029/2001JB000290.
Németh, K., Cronin, S.J., 2008. Pacific systems of a mafic island-arc volcano: Ambrym, Vanuatu, South Volcanic craters, pit craters and high-level magma-feeding. Geological Society 302. Special Publications, London, pp. 87–102. http://dx.doi.org/10.1144/SP302.6.
Neuville, D.R., 2006. Viscosity, structure and mixing in (Ca, Na) silicate melts. Chem. Geol. 229, 28–41.
Peate, D.W., Pearce, J.A., Hawkesworth, C.J., Colley, H., Edwards, C.M.H., Hirose, K., 1997. Geochemical variations in Vanuatu arc lavas: the role of subducted material and a variable mantle wedge composition. J. Petrol. 38, 1331–1358.
Pelletier, B., Calmant, S., Pillet, R., 1998. Current tectonics of the Tonga–New Hebrides region. Earth Planet. Sci. Lett. 164, 263–276.
Putirka, K., 2008. Thermometers and barometers for volcanic systems. In: Putirka, K., Tepley, F. (Eds.), Minerals, Inclusions and Volcanic Processes, Reviews in Mineralogy and Geochemistry. Mineralogical Soc. Am. 69, pp. 61–120.
Richet, P., Lejeune, A.-M., Holz, F., Roux, J., 1996. Water and the viscosity of andesitic melts. Chem. Geol. 128, 185–197.
Robin, C., Eissen, J.P., Monzier, M., 1995. Mafic pyroclastic flows at Santa Maria (Gaua) volcano, Vanuatu: the caldera formation problem in mainly mafic island arc volcanoes. Terra Nova 7, 436–443.
Sorbadere, F., Schiano, P., Métrich, N., Garaebiti, E., 2011. Insights into the origin of primitive silica-undersaturated arc magmas of Aoba volcano (Vanuatu arc. Contrib. Mineral. Petrol. http://dx.doi.org/10.1007/s00410-011-0636-1.
Sorbadere, F., Schiano, P., Métrich, N., 2013a. Constraints on the origin of nepheline-normative primitive magmas in island arcs. J. Petrol. 54, 215–233. http://dx.doi.org/10.1093/petrology/egs063.
Sorbadere, F., Schiano, P., Métrich, N., Bertagnini, A., 2013b. Small-scale coexistence of Island Arc- and enriched MORB-type basalts in the central Vanuatu Arc. Contrib. Mineral. Petrol. http://dx.doi.org/10.1007/s00410-013-0928-8.
Streck, M.J., 2008. Mineral textures and zoning as evidence for open system processes. Rev. Mineral. Geochem. 69, 595–622.
Syracuse, E.M., Abers, G.A., 2006. Global compilation of variations in slab depth beneath arc volcanoes and implications. Geochem. Geophys. Geosyst. 7 (5), Q05017. http://dx.doi.org/10.1029/2005GC001045.
Vergniolle, S., Bouche, E., 2015n. Gas-driven lava lake fluctuations at Erta Ale volcano (Ethiopia) revealed by MODIS measurements. Bull. Volcanol. (in revision).
Vergniolle, S., Jaupart, C., 1990. The dynamics of degassing at Kilauea volcano, Hawaii. J. Geophys. Res. 95/B3, 2793–2809.
Vetere, F., Behrens, H., Holz, F., Neuville, D.R., 2006. Viscosity of andesitic melts — new experimental data and a revised calculation model. Chem. Geol. 228, 233–245.
Vergniolle, S., Zielinski, C., Bani, P., Lardy, M., Le Pichon, A., Millier, P., Herry, P., Todman, S., Garaebiti, E., 2015. Listening to Ambrym Volcano (Vanuatu) by an Acoustic Array: Cyclicity in Gas Volume at an Open Vent (in preparation).
Wallace, P.J., Edmonds, M., 2011. The sulfur budget in magmas: evidence from melt inclusions, submarine glasses and volcanic gas emissions. In: Behrens, H., Webster, J. (Eds.), In Sulfur in Magmas and Melts. Reviews in Mineralogy and Geochemistry 73, pp. 215–246.
Warden, A.J., 1967. The 1963–1965 eruption of Lopevi (New Hebrides). Bull. Volcanol. 30 (1), 277–318.
Whittington, A.G., Richet, P., Linard, Y., Holtz, F., 2001. The viscosity of hydrous phonolites and trachytes. Chem. Geol. 174, 209–223.
Worster, M.G., Huppert, H.E., Sparks, R.S.J., 1990. Convection and crystallization in magma cooled from above. Earth Planet. Sci. Lett. 101, 78–89.
Worster, M.G., Huppert, H.E., Sparks, R.S.J., 1993. The crystallization of lava lakes. J. Geophys. Res. 98 (B9), 15891–15901.